

CMOS Magnetic Particle Flow Cytometer

Pramod Murali



Electrical Engineering and Computer Sciences
University of California at Berkeley

Technical Report No. UCB/EECS-2017-175

<http://www2.eecs.berkeley.edu/Pubs/TechRpts/2017/EECS-2017-175.html>

December 1, 2017

Copyright © 2017, by the author(s).
All rights reserved.

Permission to make digital or hard copies of all or part of this work for personal or classroom use is granted without fee provided that copies are not made or distributed for profit or commercial advantage and that copies bear this notice and the full citation on the first page. To copy otherwise, to republish, to post on servers or to redistribute to lists, requires prior specific permission.

Acknowledgement

I would like to express gratitude to my family, teachers and friends for their support, guidance and sacrifice. In particular, I thank my advisor Prof. Bernhard Boser for his constructive feedback and support. I also thank Prof. Ali Niknejad, Prof. Michel Maharbiz, Prof. Luke Lee, Prof. David Allstot for their valuable time and guidance.

I thank the staff of BSAC, Swarm Lab, BWRC, ERSO, IRIS of UC Berkeley particularly Abdelrahman Elhadi, Alejandro Luna, Brian Richards, Kim Ly, Mila MacBain, Patrick Hernan, Richard Lossing, Shelley Kim, Shirley Solanio, Winthrop Williams for their efficient administrative and lab support. I thank TSMC University Shuttle program for fabricating the CMOS chip. Chip fabrication by TSMC is gratefully acknowledged.

CMOS Magnetic Particle Flow Cytometer

by

Pramod Murali

A dissertation submitted in partial satisfaction of the
requirements for the degree of
Doctor of Philosophy

in

Engineering - Electrical Engineering and Computer Sciences

in the

Graduate Division

of the

University of California, Berkeley

Committee in charge:

Professor Bernhard E. Boser, Chair
Professor Ali M. Niknejad
Professor Luke P. Lee

Fall 2015

CMOS Magnetic Particle Flow Cytometer

Copyright 2015
by
Pramod Murali

Abstract

CMOS Magnetic Particle Flow Cytometer

by

Pramod Murali

Doctor of Philosophy in Engineering - Electrical Engineering and Computer Sciences

University of California, Berkeley

Professor Bernhard E. Boser, Chair

Neutrophils, a class of white blood cells, are our body's first line of defense against invading pathogens. When the number of neutrophils in blood drops to $200\text{cells}/\mu\text{L}$, it leads to a critical clinical condition called neutropenia. Currently, optical flow cytometry is the most common and powerful technique used to diagnose neutropenia, but the centralized nature of the test, time-consuming sample preparation and high cost prevent real-time modification of treatment regimens.

In this thesis, we propose an approach of using magnetic labels to tag and detect cells that allows us to design a low cost point-of-care flow cytometer to diagnose neutropenia. The cytometer cartridge integrates a gravity driven microfluidic channel with a CMOS sensor chip that detects magnetically labeled cells as they flow over it.

The sensor combines an on-chip excitation coil that magnetizes the labels and a pick-up coil that detects them. The high frequency RF signal from the sensor is down-converted and amplified by on-chip receiver circuitry, which has been optimized to maximize the signal to noise ratio. The functionality of the cytometer is demonstrated with SKBR3 cancer cells labeled with $1\mu\text{m}$ magnetic labels using streptavidin-biotin chemistry. The SKBR3 cells are used in lieu of neutrophils as they can be cultured in a laboratory setting and pose minimal bio-hazard. Furthermore, the high frequency operation of the sensor enables classification of two types of magnetic labels, which is necessary to obtain absolute cell-counts.

To my grandmother: Rangamma Narasappa

Contents

Contents	ii
List of Figures	iii
List of Tables	v
1 Introduction	1
2 Application	5
2.1 Neutrophil counting	5
2.2 System specifications	7
2.3 Summary	12
3 CMOS Cytometer Design	13
3.1 Understanding magnetic labels	13
3.2 Sensor	18
3.3 Receiver design specifications	25
3.4 Multi-frequency label detection	32
3.5 Circuit implementation	33
3.6 CMOS microfluidics integration	39
3.7 Measurement results	45
4 Conclusion	51
A Gravity Driven Flow	52
B Noise Analysis of Direct Down Conversion Receiver	54
B.1 SNR for Receiver Chain	54
Bibliography	62

List of Figures

1.1	(A) Sample preparation steps for fluorescent labeling. (B) Schematic of an optical flow cytometer.	1
1.2	(A) Sample preparation steps for magnetic labeling. (B) Schematic of magnetic label. (C) Schematic of an optical flow cytometer.	2
2.1	Different types of cells in blood [8].	5
2.2	(A) Data from a flow cytometer performing blood count. (B) A typical complete blood count scatter plot from the cytometer. The Fraction of neutrophils is obtained from this scatter plot and the neutrophil count is calculated using Eqn. 2.1 [10].	7
2.3	Flow chart to determine design requirements of a flow cytometer	8
2.4	(A) Time of flight (T_p) measurement of Dynabeads. (B) Distribution of T_p	10
2.5	Schematic of flow cytometer receive chain.	11
2.6	Background Rate vs threshold level relative to RMS noise (SNR) for the receiver shown in Fig. 2.5.	12
3.1	(A) CPW setup for measuring complex susceptibility. (B) Zoomed in image of the spiral inductor sensor wire-bonded to CPW.	14
3.2	SEM images of ferrite labels with typical size of 400 nm used for label characterization experiments.	16
3.3	(A) Complex susceptibility plot for iron oxide nano-particles. (B) Phase of complex susceptibility of different magnetic materials.	17
3.4	Phase plots of different titrations of magnetic nano-particles.	17
3.5	Variation of susceptibility with external DC magnetic field.	18
3.6	Model of the spiral transformer.	19
3.7	Noise source in a spiral sensor and its equivalent model.	20
3.8	Magnetic moment of the labelled cell as a function of excitation coil diameter.	21
3.9	Effect of number of turns in the pick-up coil on the SNR.	22
3.10	Effect of spacing between turns in the pick-up coil on the SNR.	22
3.11	Effect of width of the turns in the pick-up coil on the SNR.	23
3.12	Frequency vs. complex permittivity $\epsilon = \epsilon_r + j\epsilon_i$ for 1x PBS saline solution [21].	24

3.13	De-Qing of pick up coil in the presence of 1x PBS solution.	25
3.14	Schematic of the sensor.	26
3.15	Schematic of different blocks with the receiver chain.	27
3.16	Sensor connected to the front end with input noise referred sources $\overline{i_r^2}$ and $\overline{v_r^2}$. . .	28
3.17	Noise model for MOSFET.	28
3.18	Noise sources in a direct conversion receiver.	29
3.19	Effect of phase noise of the oscillator and divider on base-band output due to self mixing.	31
3.20	Comparison of measured and simulated input referred noise spectrum. The filtering of the measured noise after 100KHz is from the off-chip anti-alias filtering.	32
3.21	Architecture of the chip which includes the sensor, down-conversion receiver circuits and an LC oscillator.	33
3.22	Circuit schematic of oscillator.	34
3.23	Frequency divider using toggle flip-flops (T-FF) to generate in-phase (0° and 180°) and quadrature phase (90° and 270°) LO clock signals.	35
3.24	Drive circuit for excitation coil.	35
3.25	Front end amplifier circuit.	37
3.26	Schematic of passive mixer.	37
3.27	Circuit schematic of TIA and two stage differential opamp.	39
3.28	Photograph of the chip.	40
3.29	(A) Process steps for CMOS microfluidics and integration. (B) SEM image showing the interface between the CMOS chip and polystyrene. (C) Surface profile scan across the CMOS chip including the PCB and polystyrene.	41
3.30	(A) CAD model of the mold showing cavities for wire-bonds. (B) 3D printed mold used for PDMS micro-channel soft-lithography.	42
3.31	(A) Schematic of CMOS integrated with microfluidics. (B) Fabricated flow cytometer.	43
3.32	Experimental setup used for measurements.	44
3.33	Focusing of Dynabead by magnetophoresis.	45
3.34	Detection of Dynabeads by two frequency channels.	46
3.35	(A) Magnetic labeling of SKBR3 cells. (B) Detection of magnetically labeled cells by the cytometer.	47
3.36	Classification of three label classes by the flow cytometer.	48
A.1	Simplified schematic of a microchannel driven by gravity.	52
B.1	Modeling of source noise of the receiver.	56
B.2	Modeling of noise from the switches.	58
B.3	Modeling of base-band noise sources of the receiver.	60

List of Tables

1.1	Comparison of fluorescent and magnetic labeling techniques.	3
2.1	Parameters that determine T_{flow} in Eqn. 2.2	10
3.1	Different parameters for evaluating the signal from the sensor.	26
3.2	Receiver design specifications for the receiver.	31
3.3	Comparison with other chip-scale immuno-sensors and flow cytometers.	49

Acknowledgments

यस्य कृत्यं न जानन्ति मंत्रं वा मंत्रितं परे ।
कृतमेवास्य जानन्ति स वै पण्डित उच्चते ॥

Meaning: One cannot guess what a person is going to do. One cannot understand or appreciate a persons advice or the importance of the task as emphasised by him/her. Only after people (someone like me) see the fruits as a result of doing such a task then one recognises such a persons greatness, who can rightly be called a Pandit, a person esteemed for his wisdom (an advisor).

I would like to express gratitude to my family, teachers and friends for their support, guidance and sacrifice. In particular, I thank my advisor Prof. Bernhard Boser for his constructive feedback and support. I also thank Prof. Ali Niknejad, Prof. Michel Maharbiz, Prof. Luke Lee, Prof. David Allstot for their valuable time and guidance.

I thank my friends Adrien Pierre, Aamod Shanker, Andrew Townley, Arka Bhattacharya, Behnam Behroozpour, Burak Eminoglu, Chintan Thakkar, Daniel Cohen, Daniel Gerber, Efthymios Papageoriou, Filip Maksimovic, Greg Lacaille, Hao-Yen Tang, Igor Izyumin, Jacobo Paredes, Jaeduk Han, Jiashu Chen, Jun-Chau Chien, Kosta Trotskovsky, Lingkai Kong, Liyin Chen, Lucas Calderin, Marc Cooligan, Matthias Auf der Mauer, Maysamreza Chamanzar, Mervin John, Michael Lorek, Mitchell Kline, Nathan Narevsky, Nihar Shah, Nitesh Mor, Octavian Florescu, Oleg Izyumin, Paul Keselman, Po-Ling Loh, Prasanth Mohan, Rashmi K V, Richie Przybyla, Sameet Ramakrishnan, Sandeep Prabhu, Simone Gambini, Siva Thyagarajan, Sriram Venugoplan, Steven Callendar, Travis Massey, Varun Jog, Venkatesan Ekambaram, Vijay Kamble, Vikram Iyer, Yida Duan for making my graduate student life at Berkeley a memorable one.

I thank the staff of BSAC, Swarm Lab, BWRC, ERSO, IRIS of UC Berkeley particularly Abdelrahman Elhadi, Alejandro Luna, Brian Richards, Kim Ly, Mila MacBain, Patrick Hernan, Richard Lossing, Shelley Kim, Shirley Solanio, Winthrop Williams for their efficient administrative and lab support.

Chapter 1

Introduction

In the current clinical scenario, a doctor has limited diagnostic tools to quantify the health of an out-patient. These tools, often called point-of-care diagnostic instruments, include blood glucose meter, pulse oxymeter and blood pressure meter which diagnose diabetes or cardiac complications. For diagnosing many other diseases such as cancer, infections, anemia, a patient is directed to a centralized laboratory wherein trained technicians operate bench-top instruments such as centrifuge, flow cytometers and fluorescent microscopes in order to perform the necessary tests with blood/tissue samples. This process is time consuming, expensive and often requires at least two visits to the doctor (a few hours to a few days apart) to allow for the results to be available. Therefore, it will be very convenient to have a diagnostic device in a doctor's office to quickly provide relevant information about a patient's health to help him/her decide the future course of treatment.

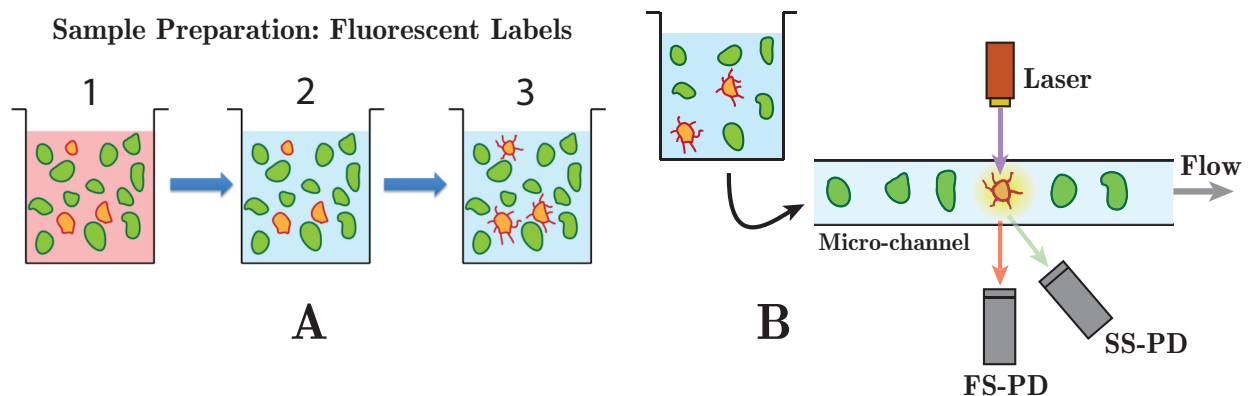


Figure 1.1: (A) Sample preparation steps for fluorescent labeling. (B) Schematic of an optical flow cytometer.

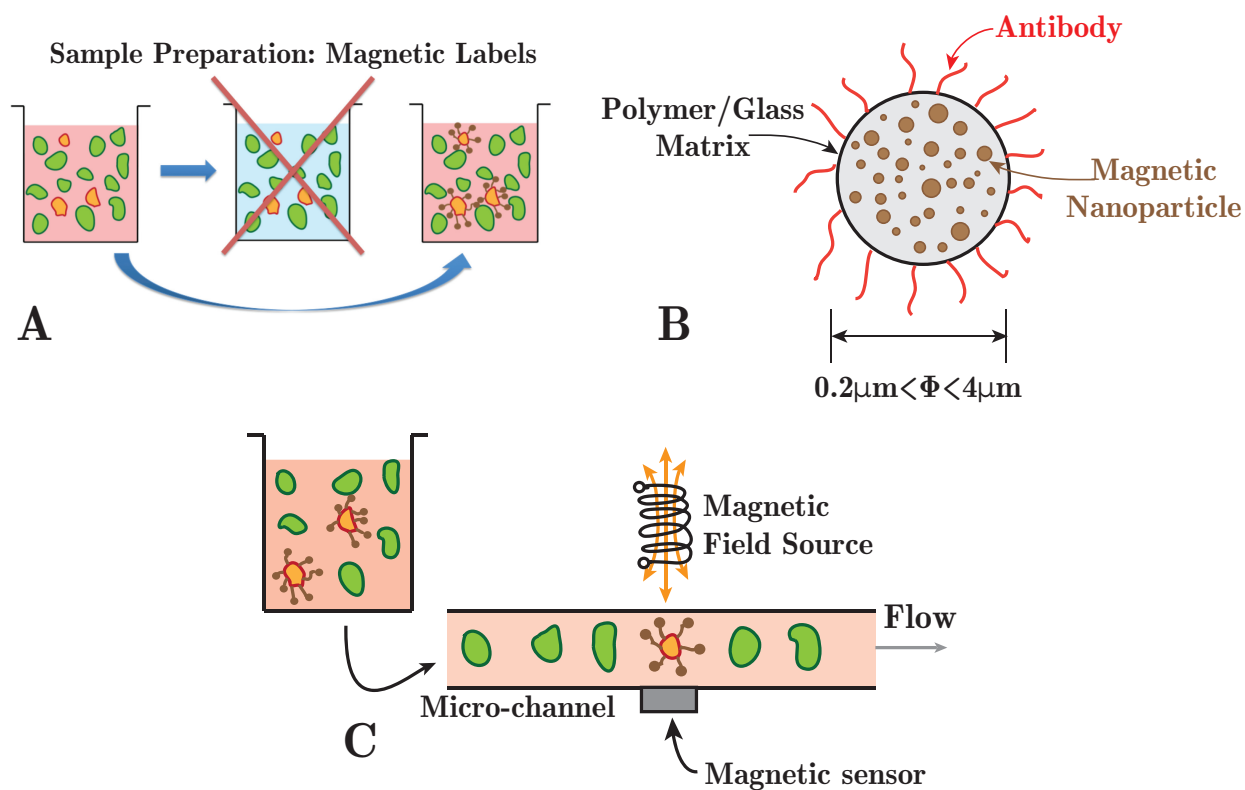


Figure 1.2: (A) Sample preparation steps for magnetic labeling. (B) Schematic of magnetic label. (C) Schematic of an optical flow cytometer.

Such a point-of-care diagnostic device should be reliable, low cost, disposable and should integrate both sensing and data processing capabilities. In this direction, CMOS and microfluidics technology, when integrated together, offers complex signal processing and sensing capabilities to meet the above requirements. Over the last thirty years, the research in CMOS bio-sensors has focused on using techniques such as impedance spectroscopy [1], capacitance change [2], magnetic Hall effect sensors [3] and cyclic voltametry [4] for detection of biomolecules such as cardiac bio-markers, DNA, glucose, lactose among many other analytes. In addition, the study of structure, number and function of specific cell types in the body is also vital for diagnosing patients. In this work, our goal is to realize a point-of-care flow cytometer to count specific cells by leveraging the advances of micro-fabrication and CMOS technology.

Current approach to flow cytometry involves (1) collection of blood sample from a patient, (2) treatment of the sample with an anti-coagulant followed by dilution, (3) labelling of the cells of interest with fluorescent molecules or staining agents and running the sample

Fluorescent Labeling	Magnetic Labeling
Optical background noise from unlabeled cells	No magnetic background noise from the sample
Requires calibration of the flow cytometer	No calibration required
Red blood cells have to be lysed and white blood cells have to be isolated from the sample	Measurement can be performed in whole blood
Requires trained users in centralized lab facilities	Enables point-of-care diagnosis

Table 1.1: Comparison of fluorescent and magnetic labeling techniques.

through a flow cytometer as shown in Fig. 1.1(A). The instrument, schematically shown in Fig. 1.1(B) contains one or more lasers that excite the fluorophors on the cells as they flow through the laser beam in a carrier fluid. The scattered and fluorescent light is amplified by photo-multipliers and eventually detected by photo-detectors. The intensity of the side scattered (SS) light depends on the granularity of the cell while the intensity of forward scattered (FS) light depends on its size and the expression of antigens on the cell surface. The nucleus of the cell is also often tagged with a fluorescent molecules such as DAPI (4',6-diamidino-2-phenylindole) to distinguish them from dead cell debris. The acquired data from the photo-detectors is subsequently processed on a computer. A limitation of this approach is that the use of fluorescent molecules requires elaborate sample preparation such as lysing for red blood cells (RBCs). This step is necessary because the RBCs will auto-fluoresce and interfere with optical measurement. An unlabeled sample of white blood cells is also used as a *control* to calibrate the instrument and to set the threshold for the photo-detectors to prevent false detection.

In this work, we propose to replace the fluorescent labels with magnetic labels to enable us to realize a point-of-care flow cytometer. Basically, a biological sample has insignificant susceptibility ($\chi \approx 10^{-5}$) compared to magnetic labels ($\chi \approx 0.1-1$) which will mitigate any background effects. In addition, the magnetic labeling process can be done in a single step as shown in Fig. 1.2(A), ie. adding labels directly to anti-coagulated whole blood unlike most fluorescent labeling process which involves a minimum of three steps: centrifugation, washing of cells to remove free bio-molecules and finally labeling with fluorescent molecules. Tab. 1.1 compares the optical and magnetic labeling approaches.

Briefly, the magnetic labels shown in Fig. 1.2(B) are made of nano-particles of magnetic materials embedded in epoxy or glass matrix. The surface of the labels are functionalized

with antibodies specific to the antigens on the surface of the cells. The setup for detecting magnetically labeled cells is similar to an optical flow cytometer as schematically shown in Fig. 1.2(C). A magnetic field source and a magnetic field sensor play the role of the laser and the photo-detector respectively. The design of such a flow cytometer involves three sub-areas to be combined together. They are:

1. Microfluidics: This involves design of the microfluidic channel for carrying the cells through the cytometer.
2. Magnetic Labels: An understanding of the magnetic labels, their material composition, susceptibility, surface functionalization, size etc.
3. Design of the sensor system to detect the magnetically labeled cells.

The design specifications for microfluidics, choice of magnetic labels and the design of the sensor system are determined by the application. These specifications include throughput (cells/sec), labeling strategy, SNR requirements, micro-channel dimensions etc. For instance, counting circulating tumor cells (CTC) in blood is often cited as an application for a point-of-care cytometer. However, the concentration of CTCs for a patient is about 1 cell in 1mL of blood [5]. There are about 4×10^6 white blood cells in 1mL of blood [6] that needs to be rejected from counting even after lysis of red blood cells. The large sample volume, the rarity of CTCs and finally the signal to noise ratio (SNR) requirements makes it inconvenient to perform CTC counting at point-of-care. On the other hand, simple hand-held coulter counters are already available for cell counting [7] but they lack the specificity necessary for classifying between cells of identical size. Considering these factors, an application that can significantly benefit from a point-of-care flow cytometer is neutrophil counting that will be presented in Chap. 2. In Chap. 3, I will present the design of a CMOS sensor chip and its integration with microfluidics and conclude this thesis in Chap. 4.

Chapter 2

Application

2.1 Neutrophil counting

About neutrophils

About 60% volume of human blood is composed of plasma and the rest of it is a mix of white blood cells (WBCs, leucocytes), red blood cells (erythrocytes) and platelets [9] as shown in Fig. 2.1 [8]. The red blood cells are responsible for carrying oxygen to different

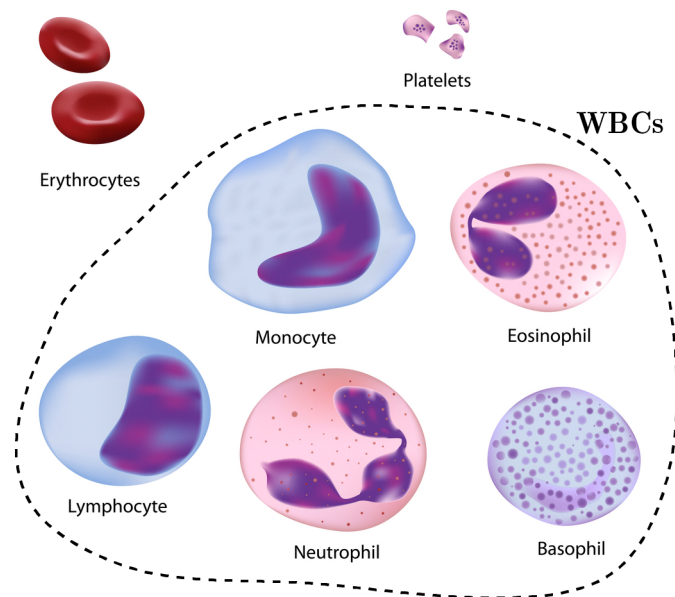


Figure 2.1: Different types of cells in blood [8].

cells in the body. The platelets are responsible for clotting of blood in case of injury and white blood cells defend the body against external pathogens. The white blood cells can be further classified into neutrophils, monocytes, lymphocytes, basophils and eosinophils. Each of these cell types have different levels of granularity, size and express different antigens on their cell surface. In particular, neutrophils are our body's first line of defense against invading bacteria and fungi and they form a significant fraction (40-75%) of WBCs. These cells are poly-nuclear that act by preferentially moving towards the site of infection and killing the pathogens by phagocytosis.

Clinical significance

In a healthy individual, the concentration of neutrophils, also called as the absolute neutrophil count, varies between 1500-8000cells/ μL of blood. Of particular interest is when the number of neutrophils drops to 200cells/ μL leading to a critical situation called *neutropenia*. Neutropenia is generally caused by chemotherapy, anemia, vitamin B-12 deficiency. and it can delay subsequent chemotherapy doses, make the patient susceptible to infections or prolonged hospitalization.

The current approach to diagnose neutropenia involves drawing about 5mL of blood from the patient and treating it with an anti-coagulant such as EDTA. The anti-coagulant binds to calcium and prevents clumping of cells in the liquid. After the collection of this sample, it is loaded into a bench-top flow cytometer to count and classify the cells in blood. The instrument automatically treats the blood sample with a lysing solution. The lysing solution contains a weak acid (like 2% acetic acid) that lyses the red blood cells and a dye such as crystal violet that labels the nucleus in the cells. Subsequently, the sample flows through a microfluidic channel and the cells are focused to the center of the channel using sheath flow. The cells are classified based on their size and internal granularity. As seen in Fig. 2.1, neutrophils are granular and larger in size compared to other white blood cells. The total number of white blood cells and the percentage of neutrophils in the scatter plot is used to determine the absolute neutrophil count.

A sample data of peripheral blood cell count obtained from an optical cytometer is shown in Fig. 2.2 [10]. The absolute neutrophil count is determined by Eqn. 2.1 using the fraction of neutrophils from the scatter plot, the volume of the sample and the total cells in it. For the data shown in Fig. 2.2, we have the total number of WBCs of 6280/ μL of blood and the percentage of neutrophils as 67.2% which gives the absolute neutrophil count as 4580/ μL of blood which is under the normal range for this patient.

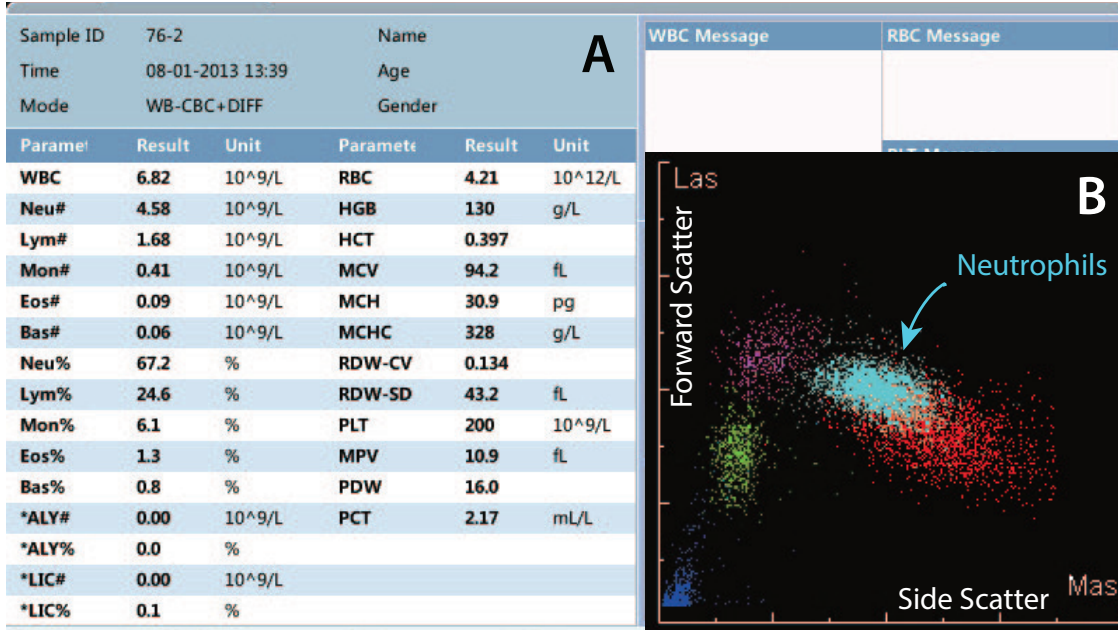


Figure 2.2: (A) Data from a flow cytometer performing blood count. (B) A typical complete blood count scatter plot from the cytometer. The Fraction of neutrophils is obtained from this scatter plot and the neutrophil count is calculated using Eqn. 2.1 [10].

$$Absolute\ Neutrophil\ Count = \frac{\% \text{ of neutrophils} \times Total\ \# \text{ of WBCs}}{100 \times Sample\ Volume} \quad (2.1)$$

Accuracy requirements

The accuracy of neutrophil counting is affected by within-patient and inter-patient biological variations ($CV \geq 7\%$) along with variation by analysis techniques. Here, CV is the *co-efficient of variation* defined as a ratio of standard deviation to the mean value. Any improvement of accuracy of a counting instrument beyond the biological variations has limited clinical significance. For neutrophil counting, it is sufficient that the accuracy $CV \leq 5\%$ [11].

2.2 System specifications

The design of a flow cytometer for neutrophil counting involves many application specific inter-dependent constraints as shown in Fig. 2.3. A measurement duration $T_{meas} \leq 2\text{min}$ is convenient for a point-of-care setting. A sample volume less than drop of blood, about

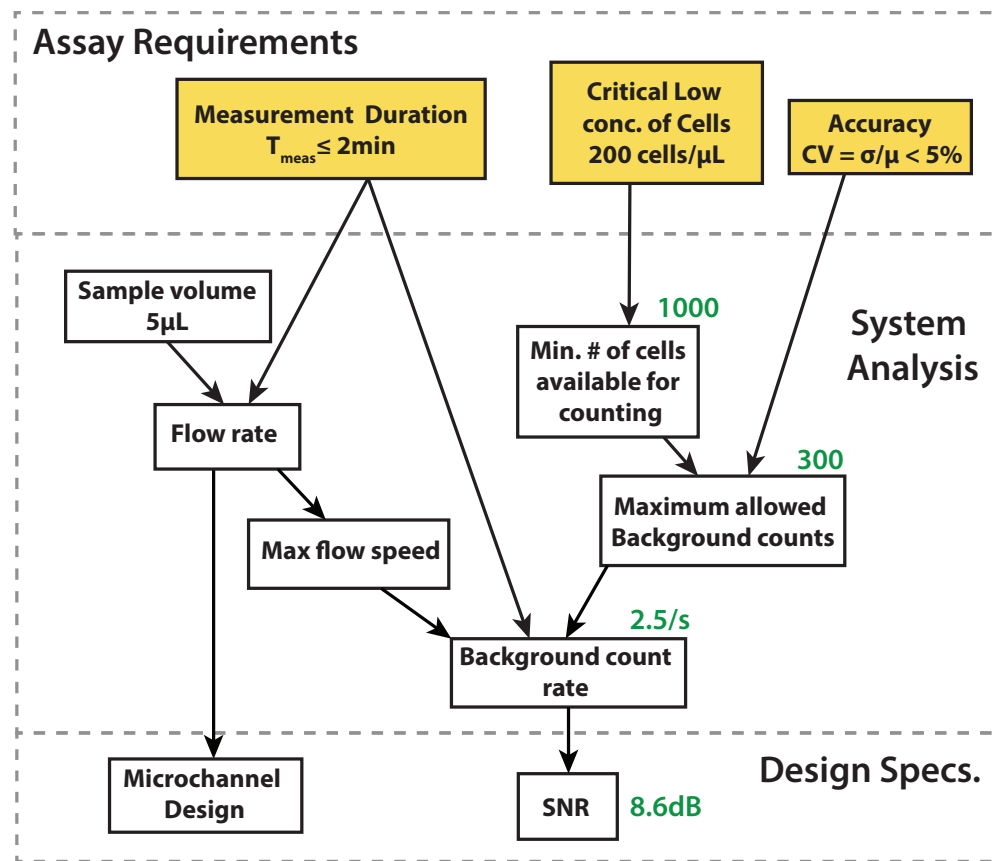


Figure 2.3: Flow chart to determine design requirements of a flow cytometer

$5\mu\text{L}$ can be collected from a finger prick and this sample contains a minimum of $N_S=1000$ neutrophils that needs to be counted with an accuracy 4-5%.

Design of microfluidics

Microfluidics is used to carry the cells through the cytometer over the sensor. The following challenges need to be addressed for a point-of-care flow cytometer.

1. Electrical isolation: The microfluidic channel should isolate the electrical connects to the sensor system from the conducting saline sample.
2. Leakage: The interface between the microfluidic channel and the sensor surface should be leak proof to prevent any loss of the sample.
3. Micro-channel shape: The commonly used technique to realize a micro-channel is by soft-lithography techniques to realize a micro-channel (typically $100 \times 200 \mu\text{m}^2$ in size)

in PDMS using SU-8 mold. The inlet and outlet (typically 1mm wide) is punched in the PDMS perpendicular to the micro-channel. In such a case, the presence of abrupt changes in the micro-channel cross-section and the transition from vertical to horizontal flow can cause the cells to settle and clog the micro-channel. A solution to this problem is to place the channel vertically with smooth transition from the inlet to the micro-channel. This can be achieved using 3D printed molds instead of SU-8 molds.

4. Fluid driving force: The driving force for the flow of sample through the microfluidic channel is typically provided by using a syringe pump. However, this approach requires that the sample is loaded to the microfluidic channel without any air bubbles to prevent flow rate fluctuations. Further, a syringe pump is bulky and consumes high power ($\approx 50\text{W}$) making it inconvenient at the point-of-care. Instead the flow through the micro-channel can be driven by gravity, obviating the need for a syringe pump. The flow rate can be controlled by suitable design of micro-channel dimensions and the channel filling rate can be minimized by surface treatment of the micro-channel. We have used gravity driven vertical flow for the design of the micro-channel considering these benefits.

The blood sample $5\mu\text{L}$ can be incubated with magnetic labels specific to neutrophils for about 10min. This sample has to flow through the cytometer in less than 2min to meet our design specification. The duration of sample flow through the channel can be divided into the time to fill the micro-channel and the time taken for the sample to completely empty through it. The time taken to fill the micro-channel is negligible compared to the time taken for the sample to completely flow through it. It can be shown that the time needed for 99% of the sample to flow through the micro-channel is given by (see Appendix A):

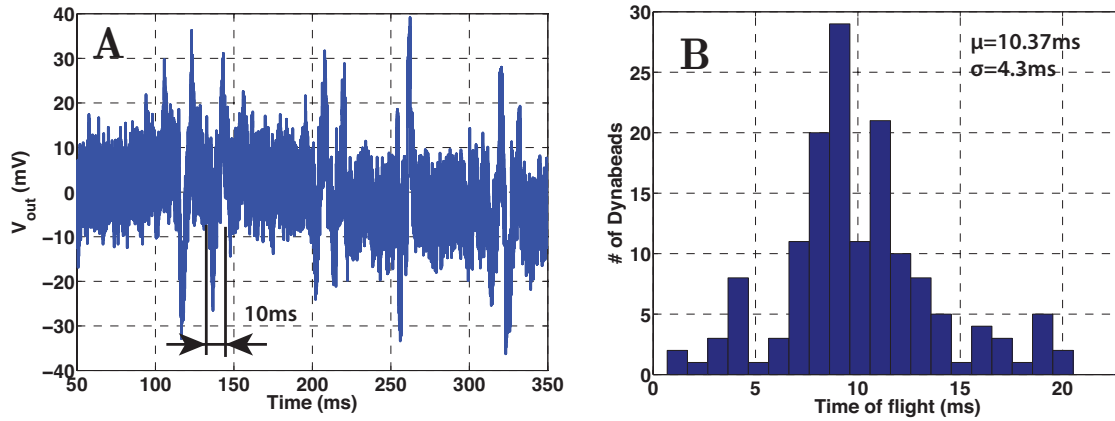
$$T_{flow} = \frac{54\eta A_{res}L}{A_{ch}\rho gh^2} \quad (2.2)$$

For the designed micro-channel dimensions shown in Fig. A.1 and Tab. 2.1, we get $T_{flow}=119\text{s}$ meeting the specification of $T_{meas} \leq 2\text{min}$. In addition, the time taken for each cell to flow over the sensor, called the *time-of-flight*, determines the duration of the match filter impulse response discussed in the next section. The shortest time of flight (T_p) of a cell over the sensor is given by

$$T_p = \frac{12D\eta L}{H\rho gh^2} \quad (2.3)$$

where D is the size of the sensor.

Parameter	Definition	Value
η	Viscosity of water	$8.9 \times 10^{-4} \text{N.s/m}^2$
A_{res}	Area of the reservoir	$0.9 \times 0.9 \text{mm}^2$
L	Length of the micro-channel	6mm
ρ	Density of water	1000Kg/m^3
g	Acceleration due to gravity	9.8m/s^2
h	Height of the micro-channel	$100 \mu\text{m}$
W	Width of the micro-channel	$200 \mu\text{m}$
A_{ch}	Area of micro-channel	$W \times h$

Table 2.1: Parameters that determine T_{flow} in Eqn. 2.2Figure 2.4: (A) Time of flight (T_p) measurement of Dynabeads. (B) Distribution of T_p .

Measurement results: It is experimentally verified that $5 \mu\text{L}$ of saline completely flows through the micro-channel in about 100s-110s. To verify the time-of-flight over the sensor, an experiment is carried out by continuously filling the reservoir with a sample containing $4.5 \mu\text{m}$ magnetic particles (Dynabeads) as cell proxies in DI-water. The time-of-flight is determined from the duration of the pulse (shown in Fig. 2.4(A)) generated by a Dynabead flowing over the sensor. Fig. 2.4(B) shows that the distribution of T_p has a mean of 10.8ms which is close to 9.1ms calculated from Eqn. 2.3. Considering that particles/cells have negligible inertia compared to fluid drag forces, their velocity closely matches the fluid velocity near the centre of the channel. However, micro-channel wall roughness, parabolic velocity profile of fluid flow, near wall effects can lead to mismatch between the measured and calculated T_p .

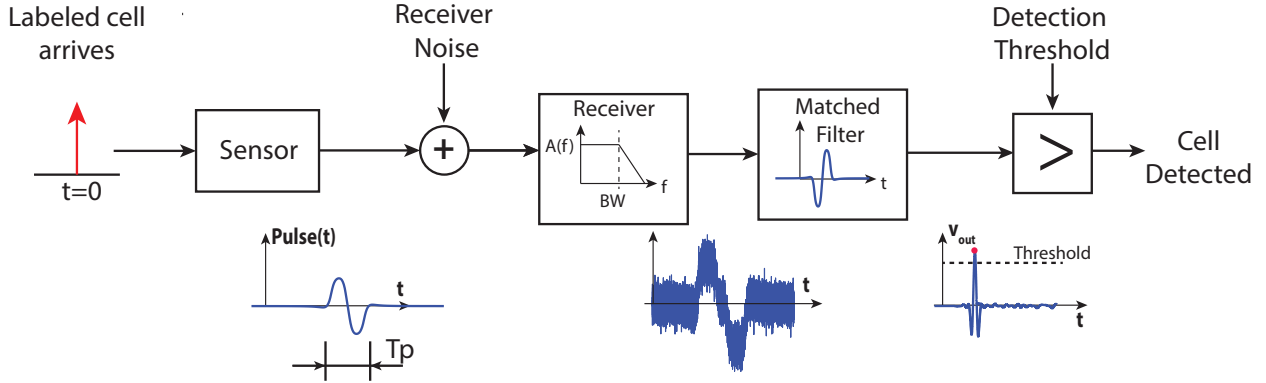


Figure 2.5: Schematic of flow cytometer receive chain.

Background count and detection threshold

To obtain the SNR requirements for the cytometer, we need to look at the complete signal path as shown in Fig. 2.5. The flow of a cell over the sensor produces a bipolar pulse at the sensor output. The pulse is then amplified by the receiver also adding undesirable noise. To maximize the SNR, the receiver output is convolved (or auto-correlated) with the expected pulse shape using a matched filter (whose impulse response is identical to the shape of the pulse from the sensor). We eventually conclude that a magnetically labeled neutrophil is detected if the match filter output exceeds a certain threshold. However, the presence of noise leads to false positives or background counts. Counting statistics from radiation detection theory can be used to determine the appropriate threshold or the minimum SNR required to meet the accuracy requirements [12].

Assume that a background count (N_B) is repeatedly measured for a fixed duration T_{meas} in the absence of any flowing cells for a certain threshold setting. Here *threshold* is defined (in dB) relative to rms noise at the match filter output. The count will be Poisson distributed with mean N_B and $\sigma_{N_B} = \sqrt{N_B}$. Now, if we repeat the experiment in the presence of cells flowing over the sensor, we will count both the background as well as the cells to obtain a total count (N_T) and $\sigma_{N_T} = \sqrt{N_T}$. N_T and N_B can then be used to determine the actual number of cells (N_S).

$$N_S = N_T - N_B \quad (2.4)$$

$$\sigma_{N_S} = \sqrt{\sigma_{N_T}^2 + \sigma_{N_B}^2} = \sqrt{N_S + 2N_B} \quad (2.5)$$

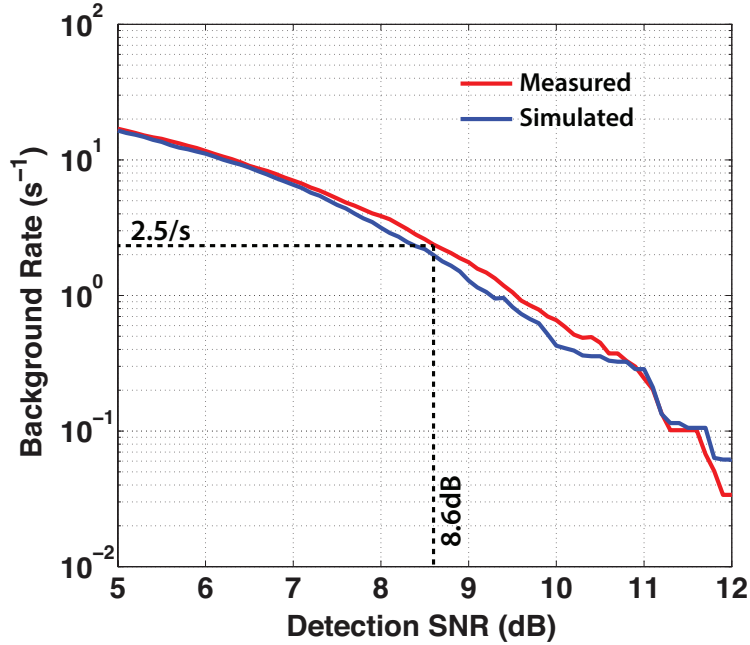


Figure 2.6: Background Rate vs threshold level relative to RMS noise (SNR) for the receiver shown in Fig. 2.5.

$$CV = \frac{\sigma_{N_S}}{N_S} = \frac{\sqrt{N_S + 2N_B}}{N_S} \quad (2.6)$$

For $CV=4\%$, we can determine the maximum background count as $N_B=300$ or a count rate of $2.5/s$ (using $T_{meas}=2\text{min}$) for $N_s=10^3$ neutrophils in the sample. Using the background count rate vs. threshold plot for our system shown in Fig. 2.6, we need SNR greater than 8.6dB (threshold) from the labeled neutrophils to meet the accuracy requirements.

2.3 Summary

In this chapter, we have understood the importance of neutrophils in defending our body against infections and the need for a point-of-care flow cytometer for diagnosing neutropenia. The system level specifications are used to design the microfluidics and to determine the SNR requirements of the receiver. The next chapter will describe the design of a CMOS sensor and receiver chip to meet the SNR requirements and also present the measured results of detecting magnetically labelled SKBR3 cells, used as proxies for neutrophils.

Chapter 3

CMOS Cytometer Design

Different sensing technologies such as magneto-resistors, superconducting quantum interference devices (SQUIDs) and Hall effect sensors are currently available for detecting small magnetic fields generated by magnetically labeled cells. Giant magneto-resistive (GMR) sensors [13] and μ Hall sensors [14], fabricated in non-standard processes, have been successfully demonstrated for magnetic flow cytometers. However, the use of CMOS technology offers the advantage of integrating the sensor with signal processing blocks such as amplifiers, A/D converters, memory within the chip at a very low cost. CMOS based Hall sensors [15] or LC tank oscillator [16] sensors either require post-processing or do not offer sufficient sensitivity necessary for a cytometer. In this chapter, we present a chip scale CMOS magnetic flow cytometer that requires no post-processing or external magnets and meets the sensitivity requirements for neutrophil counting. The sensor is a spiral transformer that detects the labels at frequencies beyond 900MHz. Therefore, it is necessary to understand their magnetic susceptibility at such high frequencies. In Sec. 3.1 we present a spiral-inductor based characterization technique to measure the susceptibility. The design of the spiral transformer sensor is presented in Sec. 3.2 and the design of the receiver for down-converting the sensor signal to base-band is presented in Sec. 3.3. Finally, experimental results are presented in Sec. 3.6.

3.1 Understanding magnetic labels

The magnetic labels are made of single domain (5-20nm) ferro-magnetic nano-particles. The thermal energy at room temperature is sufficient to randomize the net direction of magnetic moment which manifests itself as super-paramagnetic behavior. The magnetic moment within these particles aligns with the applied external magnetic field.

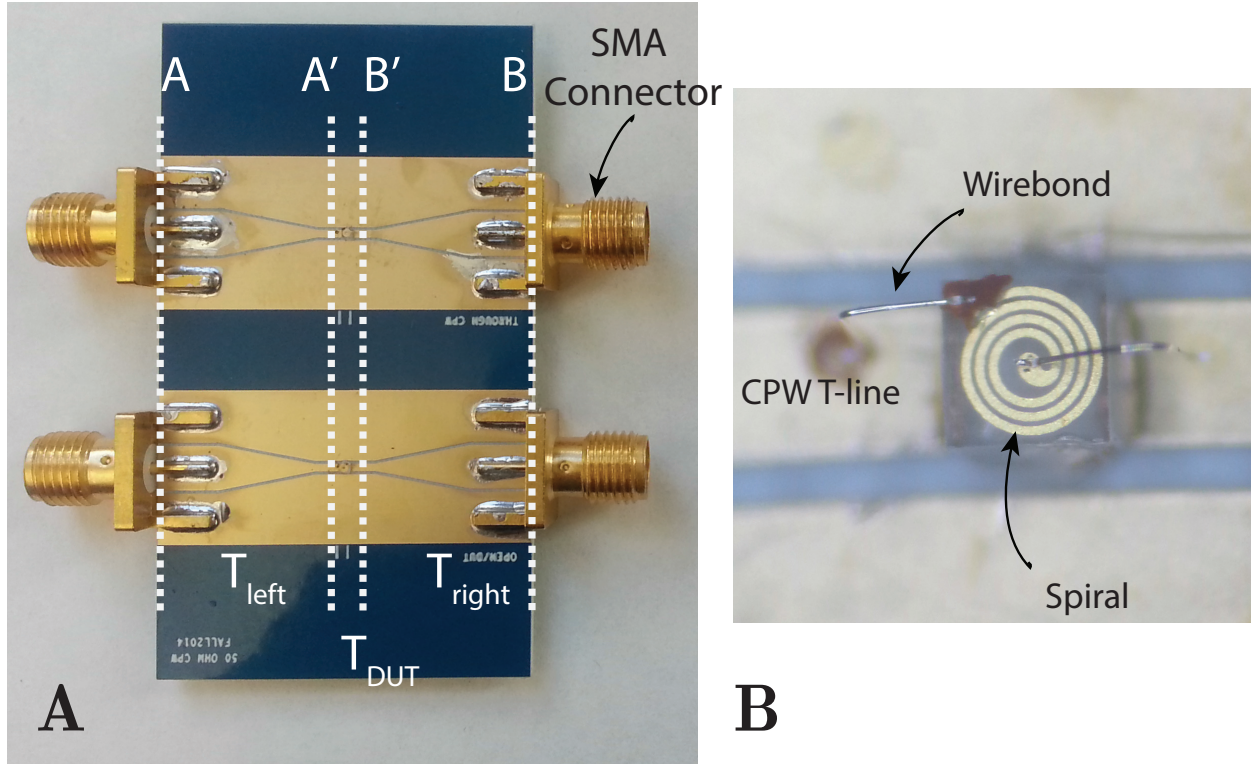


Figure 3.1: (A) CPW setup for measuring complex susceptibility. (B) Zoomed in image of the spiral inductor sensor wire-bonded to CPW.

The susceptibility $\chi = \chi' - j\chi''$ of these magnetic labels is frequency and material dependent complex number [17]. Our approach to characterize the susceptibility is to use a spiral inductor sensor and measure the change in inductance when it is immersed in these labels.

Experimental setup A 50Ω coplanar waveguide (CPW) shown in Fig. 3.1(A) is designed on a Duroid-4350 substrate. Spiral inductors fabricated on quartz substrate with nominal inductance of 4.5nH (from Piconics Inc.) are wire bonded to the transmission line as shown in Fig. 3.1(B). A vector network analyzer (E5071C, Agilent Technologies) is used for measuring the s-parameters between 500 MHz to 6GHz with 100MHz steps after performing open-short-load calibration (using C4691 ECal kit) and SMA port-extension. The IF bandwidth is set to 10 Hz and averaging factor of 16 to minimize the noise. Two port s-parameters are initially measured without the nano-particles and then 100 ng of nano-particles are dispensed on the sensor before repeating the measurements.

De-embedding and $\chi(\omega)$ extraction The waveguide has to be de-embedded from the spiral to accurately determine $\chi(\omega)$. Firstly the measured two port S-parameters (S) are transformed to T parameters are follows.

$$\begin{aligned} T_{11} &= \frac{-||S||}{S_{21}} \\ T_{12} &= \frac{S_{11}}{S_{21}} \\ T_{21} &= \frac{-S_{22}}{S_{21}} \\ T_{22} &= \frac{1}{S_{21}} \end{aligned}$$

The measured T-parameters and the simulated T-parameters of half-sections AA' (T_{left}) and BB' (T_{right}) are used to find the T-parameters of the spiral inductor sensor (T_{spiral}) as follows:

$$\begin{aligned} T_{meas} &= T_{left} * T_{spiral} * T_{right} \\ T_{spiral} &= T_{left}^{-1} * T_{meas} * T_{right}^{-1} \end{aligned} \quad (3.1)$$

T_{spiral} can be transformed to Y-parameters and $Z_{21} = 1/Y_{21}$ can be modeled as a resistor in series with an inductor ie. $Z_{21} = R_s + j\omega L$. With the nano-particles on the spiral inductor, the $Z_{21,nano}$ is given by:

$$\begin{aligned} Z_{21,nano} &= R_s + j\omega L(1 + \chi' - j\chi'') \\ &= R_s + \omega L\chi'' + j\omega L(1 + \chi') \end{aligned} \quad (3.2)$$

From $Z_{21,nano}$ and Z_{21} , the susceptibility can be obtained as follows:

$$\chi' = \frac{\Im\{Z_{21,nano} - Z_{21}\}}{\Im\{Z_{21}\}} \quad (3.3)$$

$$\chi'' = \frac{\Re\{Z_{21,nano} - Z_{21}\}}{\Im\{Z_{21}\}} \quad (3.4)$$

Absolute value of susceptibility: The magnetic labels cover the top surface of the spiral inductor and its inductance change depends on the amount of magnetic material (thickness) used. Therefore, this characterization technique can provide reliable frequency vs. normalized susceptibility data rather than the absolute susceptibility. The low frequency susceptibility measured from a different technique such as vibrating sample magnetometry [18] can be used to scale the normalized susceptibility appropriately.

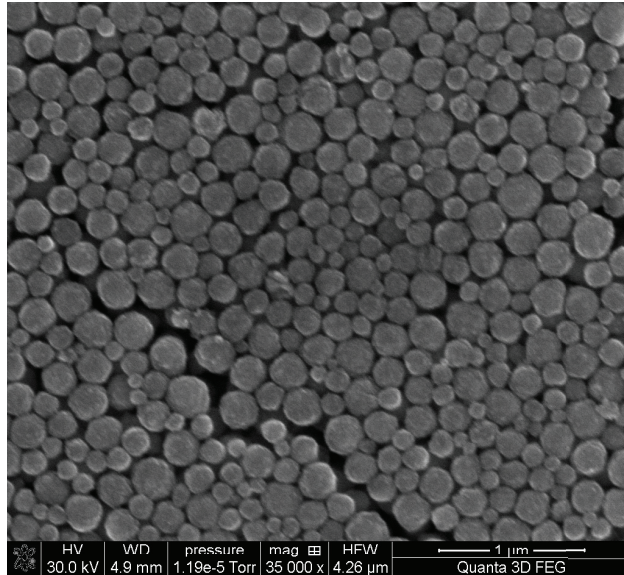


Figure 3.2: SEM images of ferrite labels with typical size of 400 nm used for label characterization experiments.

Measurement results: Five different types of magnetic nano-particles ie. ferrites of cobalt, nickle, manganese, zinc and the most commonly used iron-oxide nano-particles (Fig. 3.2) were obtained from OceanNanotech and used in our experiments. A plot of complex susceptibility of iron oxide nano-particles is shown in Fig. 3.3(A) and Fig. 3.3(B) shows a plot of the phase of the susceptibility for different types of nano-particles. The phase difference between the labels can be used for classifying as explained in Sec. 3.3. The peaking in the imaginary component of susceptibility (χ'') is due to phenomena of *ferromagnetic resonance* [17] and the corresponding frequency is a weak function of the size of nano-particles. This is unlike the *Neel's relaxation* phenomenon observed at lower frequencies (≈ 5 -100KHz) where $\chi(\omega)$ is an exponential function of the size of the nano-particles. Therefore, label classification at lower frequency using Neel's relaxation phenomenon is almost impractical considering the wide distribution of nano-particle sizes due to fabrication process variations. We also carried out measurements of different titrations of manganese ferrite and cobalt ferrite nano-particles. The phase plot of the mixtures are shown in Fig. 3.4. We see that the phase interpolates well between the phase plots of 100% of each type of nano-particles.

Verification of ferro-magnetic resonance The frequency of peaking (f_{peak}) of the imaginary component of the susceptibility increases with the increase of external applied DC magnetic field. This measurement is important to verify that the extracted susceptibility

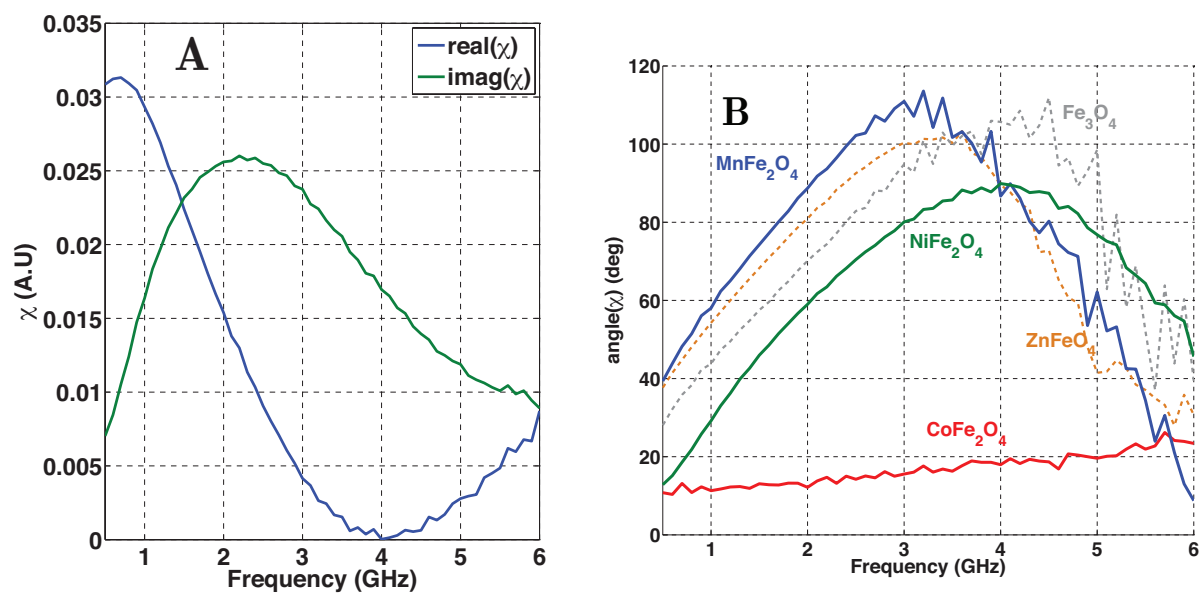


Figure 3.3: (A) Complex susceptibility plot for iron oxide nano-particles. (B) Phase of complex susceptibility of different magnetic materials.

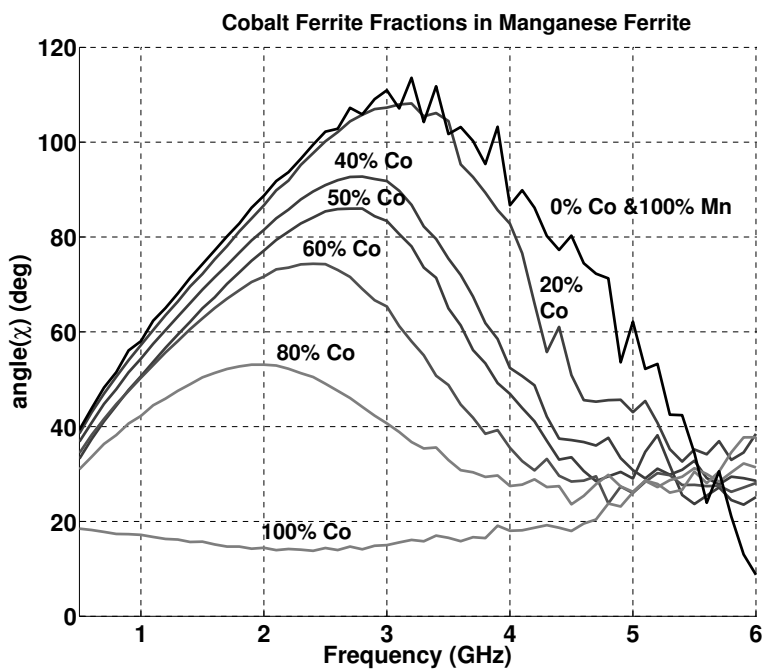


Figure 3.4: Phase plots of different titrations of magnetic nano-particles.

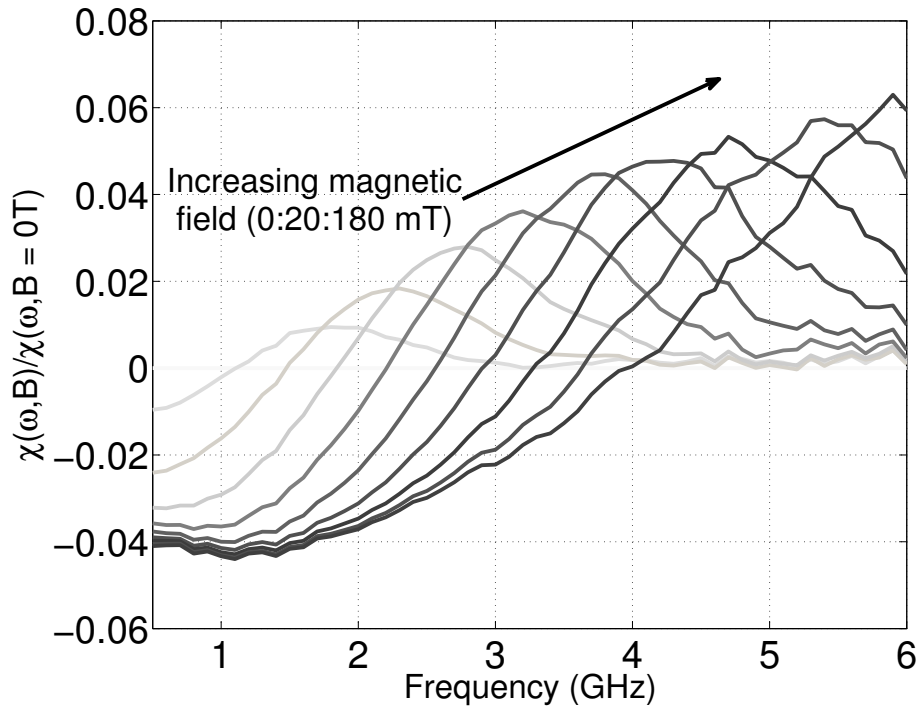


Figure 3.5: Variation of susceptibility with external DC magnetic field.

is indeed the magnetic property of the material and not a consequence of dielectric change around the spiral inductor sensor. The setup is modified to have a helmholtz coil with \vec{B} directed in the plane of the spiral. Fig. 3.5 shows variation of imaginary component of the susceptibility for different external fields $|\vec{B}|$. It can be seen that the magnitude of susceptibility and the corresponding frequency of peaking increases with increasing external magnetic field thus, verifying that our susceptibility is indeed the magnetic property of the material.

3.2 Sensor

Sensor modeling

The sensor incorporates a magnetizing coil (L_1) to magnetize the labels on the cell and a pick up coil (L_2) to sense the magnetic moment induced in the labels as schematically shown in Fig. 3.6. For our initial analysis, we use modified Wheeler expressions [19] to obtain the values spiral inductors ($L_{1,2}$). The metal conductivity and skin effect is used to determine

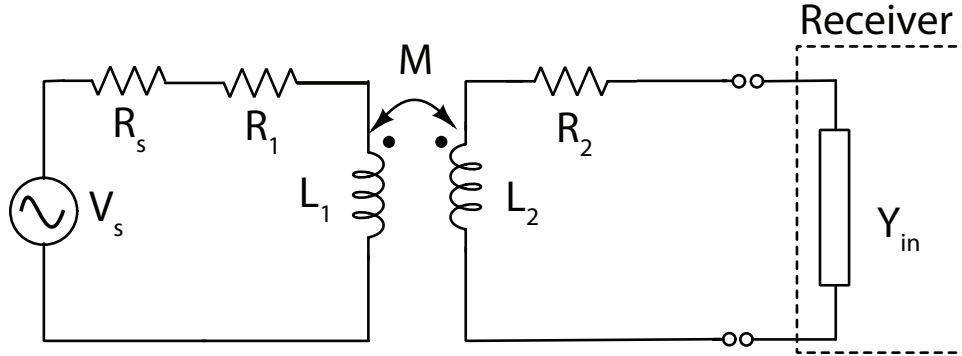


Figure 3.6: Model of the spiral transformer.

the corresponding series resistance ($R_{1,2}$) [20]. The mutual inductance (M) arises from the magnetic coupling through the labels and it can be determined as follows. The magnetic field that magnetizes the labels when the cell is located at the center of excitation spiral (L_1) can be approximated by:

$$\vec{H}_{exc} = N_1 \frac{2\sqrt{2} \cdot I_1 \hat{k}}{\pi d_1} \quad (3.5)$$

where, I_1 is the current in L_1 and N_1 is the number of metal layers, d_1 is the diameter of the loop, \hat{k} is normal to plane of the spiral. Magnetic labels, each of volume V and susceptibility (χ) when magnetized by \vec{H}_{exc} , will have a moment ($\vec{m} = \chi V \vec{H}_{exc}$) and they generate a magnetic field intensity ($\vec{B}(r)$) in the space around them.

$$\vec{B}(r) = \frac{\mu_0}{4\pi|r|^3} (3(\vec{m} \cdot \hat{r})\hat{r} - \vec{m}) \quad (3.6)$$

$\vec{B}(r)$ couples to the pick up coil (L_2) and the mutual inductance can be calculated as:

$$M = \frac{\phi_2}{I_1} \quad (3.7)$$

where,

$$\phi_2 = \sum_{j=1}^{N_2} \sum_{i=1}^P \int_{A_j} \vec{B}(r) \cdot \vec{dS}$$

A_j is the area of each loop of the N_2 loops in the pick up coil and P is the number of particles on a cell, \vec{dS} is the area element in \hat{k} direction.

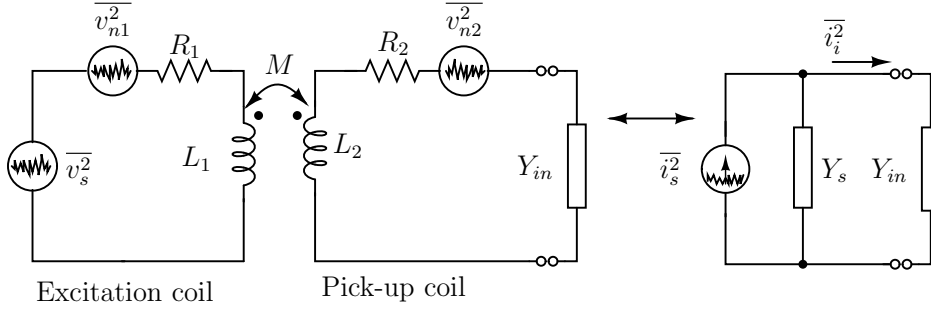


Figure 3.7: Noise source in a spiral sensor and its equivalent model.

Design considerations

Our goal is to maximize the SNR from the sensor by appropriate design of inductances $L_{1,2}$ and mutual inductance M . Fig. 3.7 shows the different noise sources in the sensor, v_{ns} is the thermal noise generated by the buffers driving the excitation coil L_1 and $v_{n1,n2}$ is thermal noise from the resistance $R_{1,2}$. It will be convenient to combine all the noise sources into i_s and equivalent source admittance Y_s . It can be shown that:

$$i_s = \frac{j\omega M(v_{ns} + v_{n1}) + v_{n2}(R_1 + j\omega L_1)}{(R_1 + j\omega L_1)(R_2 + j\omega L_2) + \omega^2 M^2} \quad (3.8)$$

$$Y_s = \frac{(R_1 + j\omega L_1)}{(R_1 + j\omega L_1)(R_2 + j\omega L_2) + \omega^2 M^2} \quad (3.9)$$

The sensor will be connected to a receiver front-end having input admittance Y_{in} as shown in Fig. 3.7.

For simplicity, if we assume that the Q of excitation and pick up coils are large, using Eqn. 3.8, Eqn. 3.9, the noise ($\overline{i_{i,noyse}^2}$) to signal ($\overline{i_{i,sig}^2}$) ratio is given by:

$$\frac{N}{S} = \frac{\overline{i_{i,noyse}^2}}{\overline{i_{i,sig}^2}} = \frac{L_1}{k_c^2 L_2} \frac{\overline{v_{n2}^2}}{\overline{v_{sig}^2}} + \frac{\overline{v_{ns}^2} + \overline{v_{n1}^2}}{\overline{v_{sig}^2}} \quad (3.10)$$

where $k_c = M/\sqrt{L_1 L_2}$ is the coupling co-efficient, $\overline{v_{sig}^2}$ is the voltage source that drives the excitation coil. The following observations can be made from Eqn. 3.10:

- From the first term in Eqn. 3.10, we can see that a higher coupling coefficient (k_c) improves the SNR. The coupling co-efficient depends on the amount of magnetic material on the cell, the susceptibility and the separation of the cell from the excitation/pick up coil.

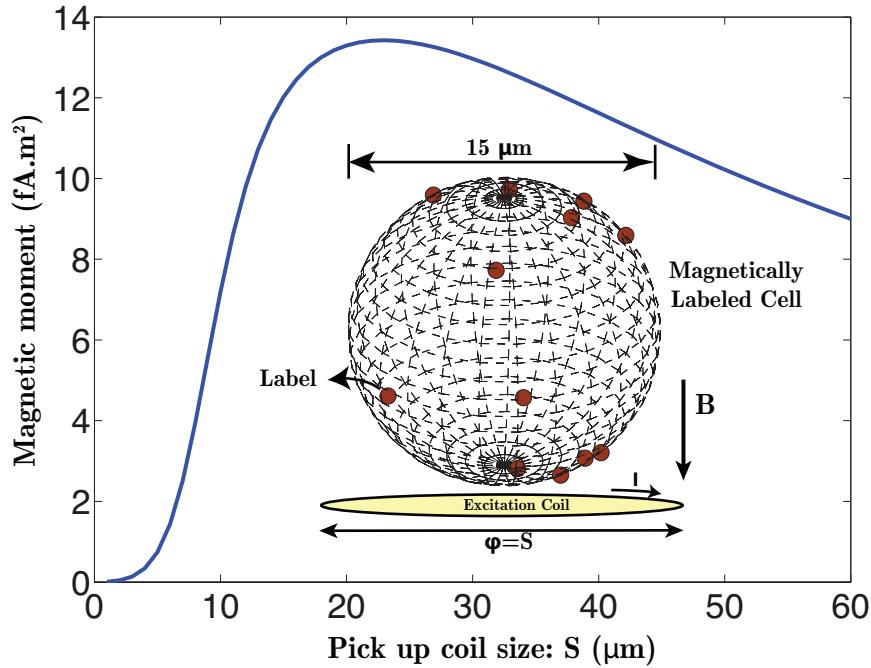


Figure 3.8: Magnetic moment of the labelled cell as a function of excitation coil diameter.

- Further, smaller excitation coil inductance (L_1) leads to a higher current through it and therefore a larger magnetic field will be generated to magnetize the labels.
- A large pick up coil inductance (L_2) increases the induced voltage for a given magnetic field from the labels. However, $\overline{v_{n2}^2}$ also increases due to increase in the series resistance.
- Finally, the noise from the excitation source $\overline{v_{ns}^2}$ and excitation coil resistance $\overline{v_{n1}^2}$ has a direct impact on the SNR.

Other sensor design considerations

Excitation coil size: From Eqn. 3.5 we see that the magnetic field strength increases by reducing the size of excitation coil. However, if the size is significantly smaller than the size of the cell, not all the magnetic labels get magnetized. Fig. 3.8 shows the total magnetic moment induced in a cell decorated with 12 of $1\mu\text{m}$ labels ($\chi=0.1$) due to the magnetic field generated by a current carrying loop (100mA) as a function of its size. It can be seen that the optimum size to maximize the moment is to choose the sensor diameter close to the size of a cell, which is $15\mu\text{m}$ for neutrophils.

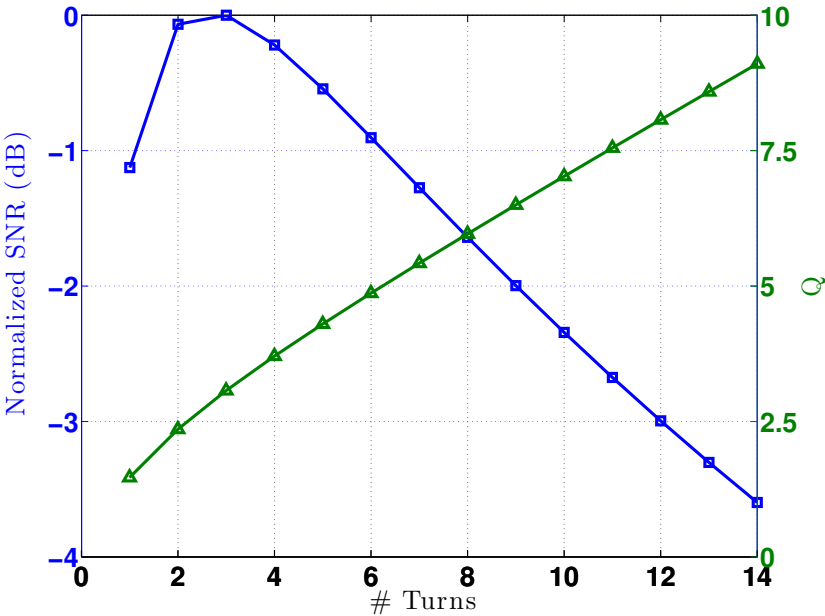


Figure 3.9: Effect of number of turns in the pick-up coil on the SNR.

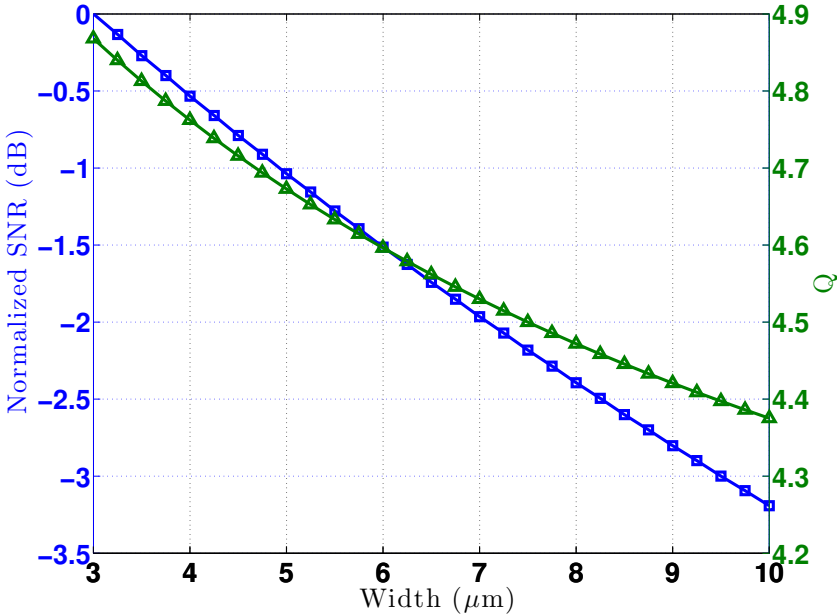


Figure 3.10: Effect of spacing between turns in the pick-up coil on the SNR.

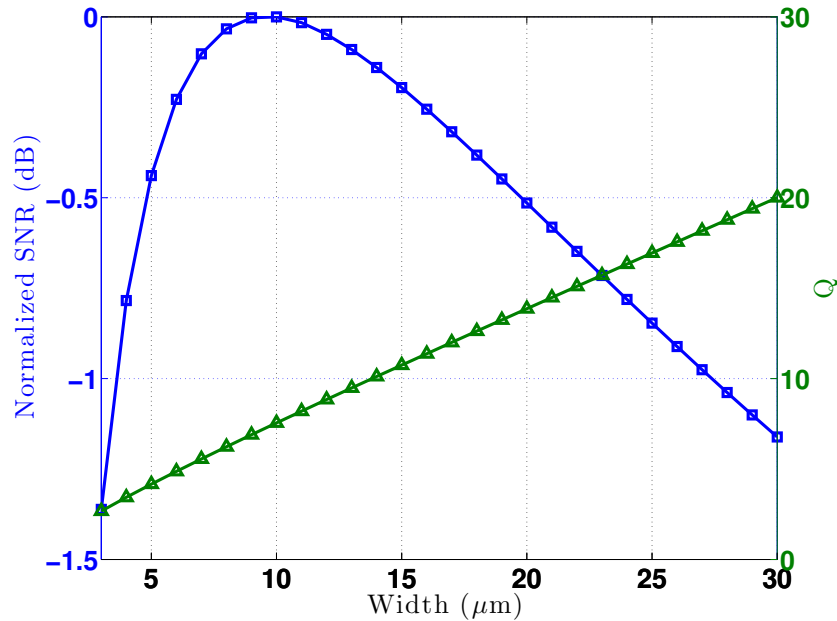


Figure 3.11: Effect of width of the turns in the pick-up coil on the SNR.

Pick-up coil size: The width, spacing between turns and the number of turns of the pick-up coil (L_2) impacts the SNR from the Sensor. With increasing number of turns in the pick-up spiral the magnetic flux picked up by L_2 increases with diminishing returns moreover the series resistance R_2 increases linearly with the number of turns. From Fig. 3.9 we see that three turns gives maximum SNR from the sensor. However, larger number of turns increases the inductance and the quality factor of the inductor. A higher Q is necessary for boosting the voltage signal at the input of the front-end amplifier. We have chosen six turns with in our design which causes only 0.5dB penalty in SNR.

From Fig. 3.10 we see that reducing the spacing between turns increases the SNR and the minimum spacing is limited only by the technology. Fig. 3.11 shows the effect of width of a turn on the SNR. We can see that the maximum SNR is achieved for a width of $10\mu\text{m}$. In this model, the effect of substrate losses on degradation of Q is not included. We have chosen a width of $6\mu\text{m}$ to minimize the sensor area which impacts the SNR by less than 0.3dB.

Amount of magnetic labels on a cell: The binding of magnetic labels on the cell is an event governed by diffusion of labels to the cells, steric-hindrance effects, brownian-motion of the labels, etc. The amount of magnetic material bound on the cell also depends on the

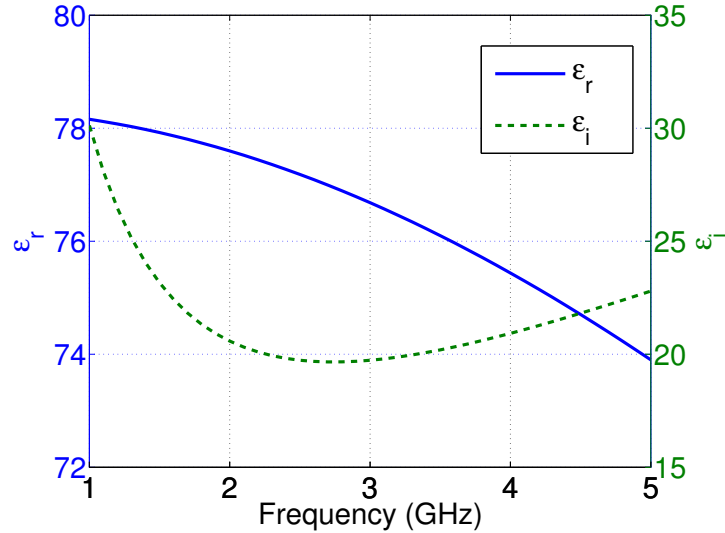


Figure 3.12: Frequency vs. complex permittivity $\epsilon = \epsilon_r + j\epsilon_i$ for 1x PBS saline solution [21].

antigen expression, cell culture conditions, pH of the labeling buffer solution, temperature etc. The variability in the labeling process coupled with the uncertainty in the absolute value of the susceptibility (see Sec. 3.1) makes it challenging to estimate the value of mutual inductance (M). Assumptions, such as the number of labels bound to a cell or the approximate value of susceptibility are inevitably made in order to determine the mutual inductance and consequently the SNR from the sensor.

Loss from saline at high frequencies: The cells are carried over the sensor in a saline solution also called the phosphate buffered saline (PBS). The presence of dissolved salts causes high frequency loss and de-Qing of the spiral inductors. We have modeled the dielectric properties of saline using semi-empirical expressions in [21] and Fig. 3.12 shows the frequency vs. complex permittivity $\epsilon = \epsilon_r + j\epsilon_i$ for 1x PBS solution used in our cell experiments. Fig. 3.13 shows the effect (simulated in HFSS) of saline solution on the Q of the pick-up coil.

Sensor implementation

Using the insights gained from the analytical models described in previous sections, a spiral sensor is implemented as shown in Fig. 3.14. It consists of a differential magnetizing coil (L_1) embedded within a pick up coil (L_2). The magnetizing coil is a three-layer, single turn

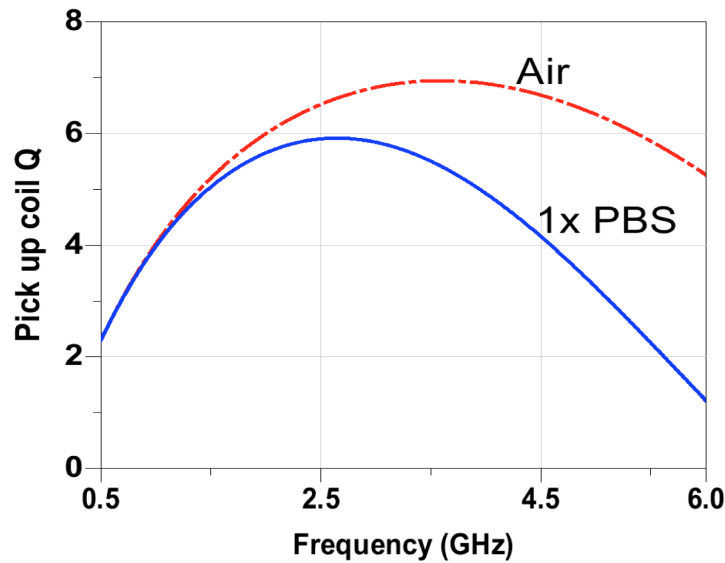


Figure 3.13: De-Qing of pick up coil in the presence of 1x PBS solution.

per layer spiral inductor implemented on the top three metal layers of the CMOS chip and has an inductance of 490pH. The inner diameter is $15\mu\text{m}$ which is comparable to the size of a typical neutrophil and the width is $6\mu\text{m}$ to limit the temperature raise from joule heating to less than 15°C in air for a 100mA current. The excitation coil generates a magnetic field density of 9.4mT (simulated) at the centre. A center tap is provided for DC biasing the excitation coil driver circuit.

The pick up coil (L_2) is a symmetric six turn spiral implemented on top two metal layers connected in parallel and it has an inductance of 4.87nH. Minimum width and spacing between turns, limited by process technology, maximizes the flux picked up from the labels. Adding more turns for larger flux pickup is compromised by thermal noise from series resistance and overall size of the coil. The sensitivity of the sensor is 0.14V/mT/GHz (simulated). The bipolar pulse shape from the sensor as the cell flows over it is shown in Fig. 3.14. Tab. 3.1 shows the estimated output form the sensor for a magnetically labelled cell.

3.3 Receiver design specifications

The RF signal from the pick coil needs to be down-converted to base-band for further amplification, digitization and processing. Among different receiver architectures, a direct down conversion receiver offers low power, low cost and high level of integration [22, 23]. The direct conversion receiver translates the RF frequency signal directly to zero intermediate

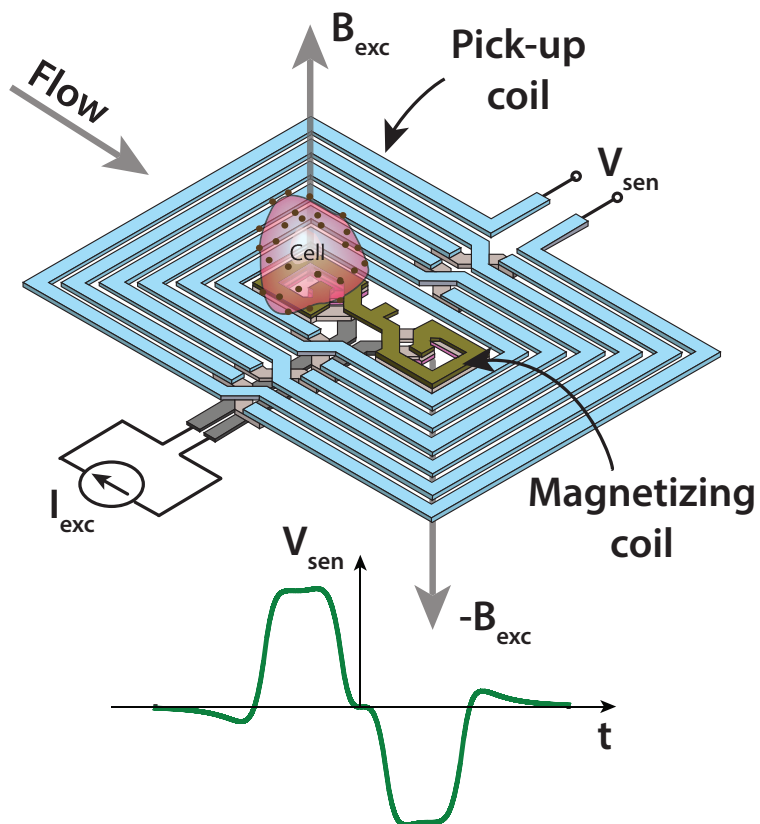


Figure 3.14: Schematic of the sensor.

Parameter	Value
Magnetic label size	$1\mu\text{m}$
Cell diameter	$15\mu\text{m}$
Number of labels on a cell	12
Susceptibility	0.1
Sensor output voltage	$2.2\mu\text{V}/\text{GHz}$

Table 3.1: Different parameters for evaluating the signal from the sensor.

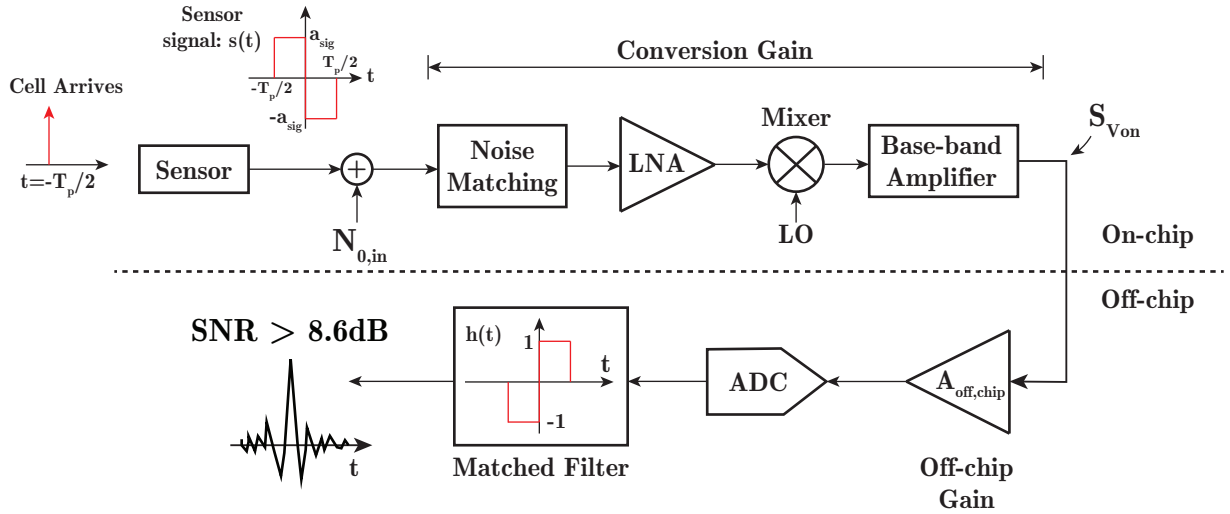


Figure 3.15: Schematic of different blocks with the receiver chain.

frequency. In our application, since the strength of the signal from the sensor is mainly determined by the small amount of magnetic material that can bind to a cell, the main focus of this work is to optimize the receiver noise performance. The complete signal chain from the sensor to the matched filter for a direct down conversion receiver is shown in Fig. 3.15.

For the purpose of analysis, the signal pulse shape can be approximated by a bipolar rectangular pulse as shown in Fig. 3.15. For a signal amplitude a_{sig} at the output of the sensor and an input referred single sided thermal noise spectral density $N_{0,in}$, it can be show that the SNR at the output of the matched filter is given by (see Appendix. B):

$$SNR = \frac{a_{sig}}{\sqrt{0.693N_{0,in}f_c}} \quad (3.11)$$

where f_c is the flicker noise corner frequency of the noise spectrum. From Sec. 3.2, for a signal $a_s = 2\mu\text{V}$ at 0.9GHz, we get an SNR of 24.5dB for input referred noise spectral density of $N_{0,in}=(1.43\text{nV}/\sqrt{\text{Hz}})^2$ and flicker noise corner of 10KHz. However, the undesired capacitive coupling between the excitation coil and pick up coil increases the flicker noise corner to 100KHz and thermal noise floor to $2.77\text{nV}/\sqrt{\text{Hz}}$ (discussed later) lowering the SNR to 9.1dB.

The effect of ADC quantization noise is minimized by appropriate design of off-chip gain ($A_{off,chip}$). The phase difference between the excitation signal and signal from the sensor (due to the complex susceptibility) necessitates an I/Q down-conversion receiver to fully recover the signal (not shown in Fig. 3.15).

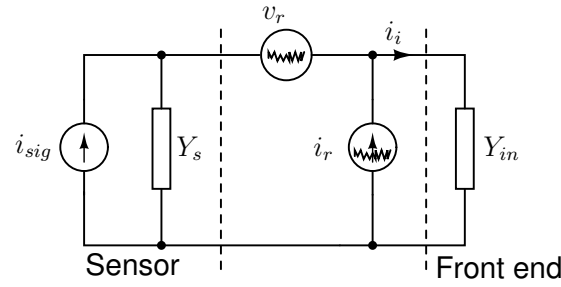


Figure 3.16: Sensor connected to the front end with input noise referred sources $\overline{i_r^2}$ and $\overline{v_r^2}$.

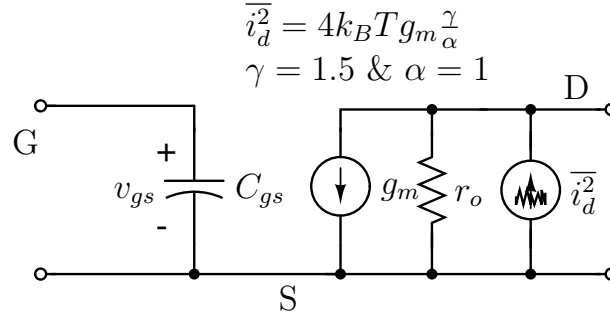


Figure 3.17: Noise model for MOSFET.

Front end noise matching

We have looked at the different noise sources of the sensor in Sec. 3.2. Here, let us consider the noise of the receiver front-end as shown in Fig. 3.16. The goal is to minimize the noise contribution from the front end circuit. Here $\overline{i_r^2}$ and $\overline{v_r^2}$ are correlated noise sources of the receiver such that $i_r = Y_c v_r$ where Y_c is the correlation coefficient. The noise to signal ratio at the input of the front end will be:

$$\frac{N}{S} = \frac{\overline{i_{i,noise}^2}}{\overline{i_{i,sig}^2}} = \frac{\overline{v_r^2}}{\overline{i_{sig}^2}} |Y_c + Y_s|^2 \quad (3.12)$$

From Eqn. 3.12, we can improve the SNR by either reducing $\overline{v_r^2}$ which translates to increasing the power consumption in the front end amplifier or by reducing $|Y_c + Y_s|^2$ as discussed below.

To find Y_c , consider the MOSFET front end with a simple noise model as shown in Fig. 3.17. Using the instantaneous noise currents from the MOSFET (i_d) we get,

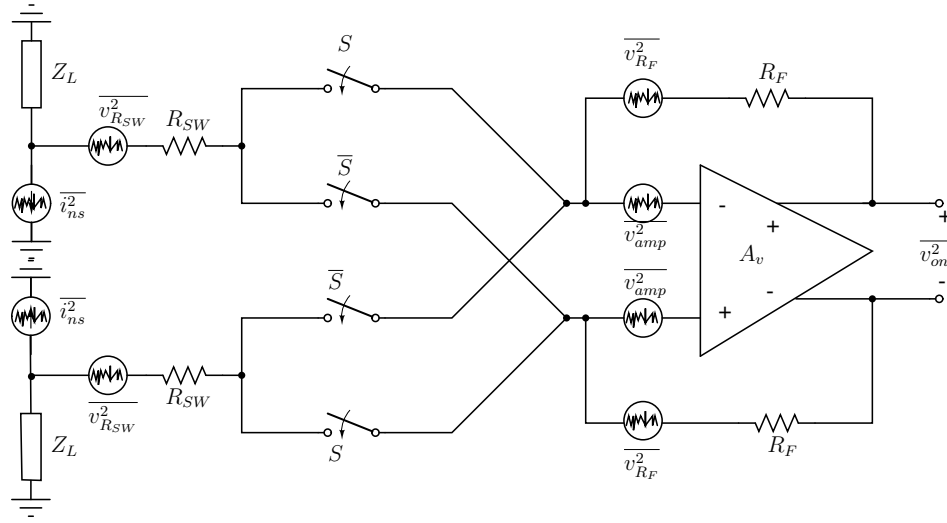


Figure 3.18: Noise sources in a direct conversion receiver.

$$\begin{aligned}
 i_r &= \frac{j\omega C_{gs}}{g_m} i_d \\
 v_r &= \frac{i_d}{g_m} \\
 Y_c &= \frac{i_r}{v_r} = j\omega C_{gs}
 \end{aligned} \tag{3.13}$$

From Eqn. 3.13 we see that Y_c is a small capacitive admittance (positive). However, from Eqn. 3.12, we want to reduce $|Y_c + Y_s|^2$ for improving the SNR (Y_s is the inductive admittance (negative) of the pick up coil). We can do this by increasing Y_c by adding a capacitor (C_{add}) in parallel to C_{gs} such that the pick up coil will resonate with the total capacitance ($C_{gs} + C_{add}$) at the frequency of operation. In other words, this additional capacitance will effectively Q boost the voltage induced in the pick up coil at gate of the front end transistors.

Noise analysis of the receiver

Fig. 3.18 shows the different noise sources in a direct down-conversion receiver. The thermal noise contribution from the sensor and the front end is combined into i_{ns}^2 . $v_{R_{SW}}^2$ is the noise of the mixer switches, v_{amp}^2 is the input referred noise of the base-band amplifier and $v_{R_F}^2$ is thermal noise of the feedback resistor. The thermal noise power spectral density at the

output of the receiver is given by (see Appendix. B):

$$S_{v_{on}} = 2\overline{v_{R_F}^2} + 2\left(1 + \frac{R_F}{Z_L + R_{SW}}\right)^2 \overline{v_{amp}^2} \quad (3.14)$$

$$+ \left|\frac{2R_F}{Z_L + R_{SW} + R_F/A_v}\right|^2 \left(\frac{1}{4} + \frac{2}{\pi^2}\right) \overline{v_{R_{SW}}^2} + \left|\frac{2R_F Z_L}{Z_L + R_{SW} + R_F/A_v}\right|^2 \left(\frac{2}{\pi}\right)^2 \overline{i_{ns}^2}$$

From Eqn. 3.14, we can make the following observations.

- The noise from the feedback resistor R_F directly adds to the output.
- The ratio of R_F and $Z_L + R_{SW}$ determine the contribution of base-band amplifier noise ($\overline{v_{amp}^2}$) to the output. It is desirable that the output impedance (Z_L) of the front end amplifier (voltage to current converter) is high. However, Z_L is dominated by the drain node parasitic capacitance and output resistance (r_0) of the transistors.
- The contribution of noise from the switch resistance ($\overline{v_{R_{SW}}^2}$) is also determined by ratio of R_F and $Z_L + R_{SW}$.
- $\overline{i_{ns}^2}$ is commonly the most dominant source of noise, therefore, it is essential to minimize the noise contribution from the front end low noise amplifier.

The input referred thermal noise spectral density can be determined using the conversion gain as follows:

$$N_{0,in} = \frac{S_{v_{on}}}{(Conv. Gain)^2} \quad (3.15)$$

where,

$$Conv. Gain = \left(\frac{2}{\pi}\right) \left(\frac{R_F Z_L g_m}{Z_L + R_{SW} + R_F/A_v}\right) \frac{Y_s}{Y_s + Y_{in}} \quad (3.16)$$

g_m is the trans-conductance of the front end amplifier. For the design parameters shown in Tab. 3.2, the input referred noise floor from Eqn. 3.15 with excitation coil off ($1.27\text{nV}/\sqrt{Hz}$) compares well with the device level SPICE simulations ($1.43\text{V}/\sqrt{Hz}$). However, the noise floor will increase when the excitation coil is turned ON as discussed in the next section.

Self mixing and sensor non-ideality

The presence of undesirable capacitive coupling between the excitation coil or the LO path and the pick up coil causes degradation of SNR. For simplicity, let us suppose that the local oscillator is a sinusoidal signal ($s_{LO}(t)$) with phase noise ($\phi_n(t)$), the phase noise can arise from oscillator and the divider circuits.

Design specification	Value
A_v	50dB
R_{SW}	10 Ω
Z_L	450 Ω
R_F	5K Ω
g_m	20mS
Conversion Gain	161

Table 3.2: Receiver design specifications for the receiver.

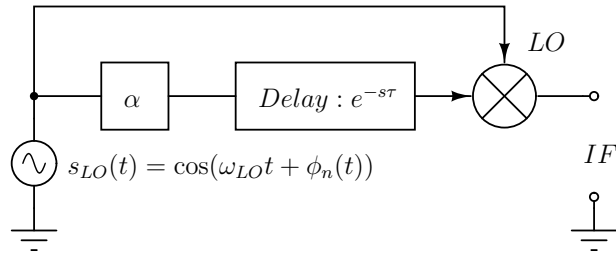


Figure 3.19: Effect of phase noise of the oscillator and divider on base-band output due to self mixing.

$$s_{LO}(t) = \cos(\omega_{LO}t + \phi_n(t)) \quad (3.17)$$

Let a factor α quantify the amount of capacitive coupling between the excitation coil/LO path with the pick up coil and τ denote the delay between the excitation signal and mixer LO signal. The low frequency output of the mixer, will be:

$$\begin{aligned} IF &= \alpha s_{LO}(t) s_{LO}(t - \tau) \\ &= \frac{\alpha}{2} \cos(\omega_{LO}\tau + \phi_n(t) - \phi_n(t - \tau)) \end{aligned} \quad (3.18)$$

Unless $\tau = 0$, the phase noise will get down-converted to base-band and appear as amplitude noise at the receiver output degrading the SNR. The value of τ and α depends on the layout design, device parameters etc. which can be only be estimated by post-extraction simulations.

Fig. 3.20 shows the simulated (post extraction) input referred noise spectrum from the chip ($N_{in,0}$), with and without the coupling between the excitation coil and the pick up coil. The input referred noise floor goes up from 1.43nV/ \sqrt{Hz} to 2.77nV/ \sqrt{Hz} and flicker corner from 10KHz to \approx 100KHz. Fig. 3.20 also shows the measured noise spectrum that includes both coupling from excitation coil and the LO path. It should be noted here that even

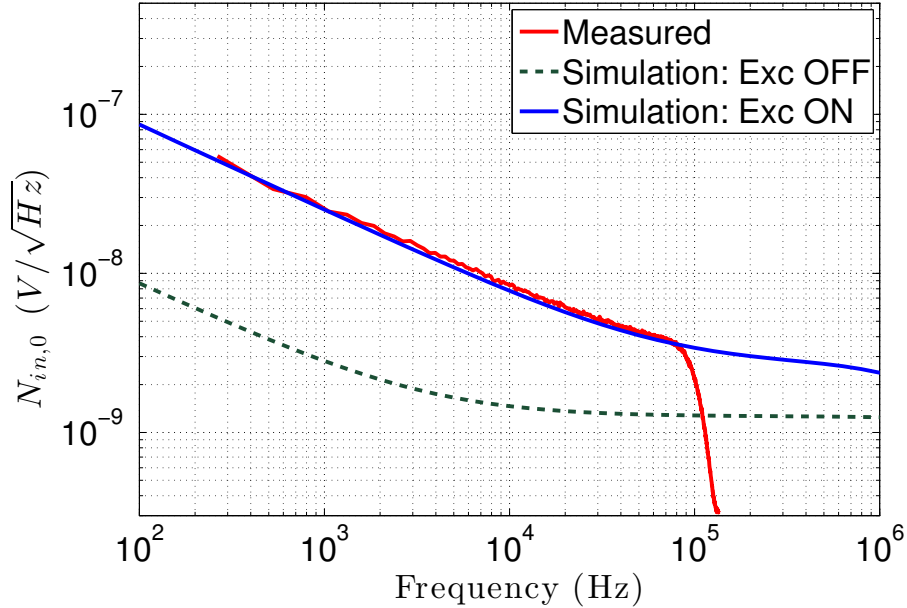


Figure 3.20: Comparison of measured and simulated input referred noise spectrum. The filtering of the measured noise after 100KHz is from the off-chip anti-alias filtering.

though the excitation coil could be turned OFF by setting $V_{drive}=0$ during measurements, the LO coupling cannot be turned OFF to compare the measurements with simulations for “Excitation OFF” situation.

3.4 Multi-frequency label detection

With two or more sensors operating at the same frequency but are separated spatially provides an SNR improvement of \sqrt{N} (where N is the number of sensors) [24]. Moreover, the flow of cells in the micro-channel is affected by its interaction with the micro-channel walls, chip surface roughness etc. Even with on-chip magneto-phoresis, the vertical separation from the chip surface cannot be well controlled. Having multiple detection sites increases the probability of detecting a cell missed by any given sensor. In addition, if we operate the sensors of the array at different frequencies, there are two other benefits.

Firstly, the signal from the sensor scales linearly with the frequency of operation. This is particularly beneficial for cobalt like nano-particles where the magnitude of susceptibility is almost a constant between 1-5GHz. Secondly, in medical diagnostics, the non-specificity of antibody-antigen binding decreases the confidence of identifying a particular cell. For in-

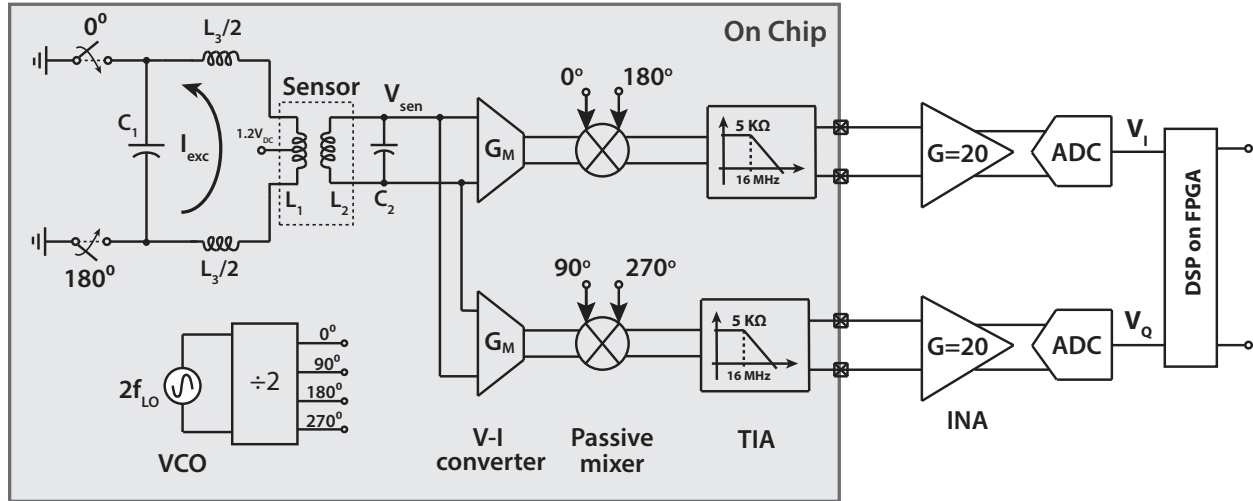


Figure 3.21: Architecture of the chip which includes the sensor, down-conversion receiver circuits and an LC oscillator.

stance, CD15 and CD16 antigens are strongly expressed by neutrophils [25], however the corresponding antibodies anti-CD15 or anti-CD16 can non-specifically bind to B-cells or T-cells. Therefore, cobalt ferrite functionalized with anti-CD15 and manganese-ferrite functionalized with anti-CD16 can be used to identify neutrophils with a higher confidence compared to using a single antibody. The phase data shown in Fig. 3.4 can be used to determine the relative expression of CD15 and CD16 thereby increasing the confidence in concluding that the detected cell is indeed a neutrophil. From Fig. 3.4 we can also see that the maximum phase difference between magnetic particles occurs between 2.5-3.5GHz which is appropriate frequency to operate one of the sensors. In our experiments, we have used two of the four available frequency channels ie. 0.9GHz and 2.6GHz.

3.5 Circuit implementation

The complete architecture of the receiver is shown in Fig. 3.21. The oscillator, sensor and receiver are integrated within the chip. Each of the individual blocks are described in the following sections.

Oscillator The oscillator is implemented using an LC tank connected to a pmos based negative transconductance stage as shown in Fig. 3.22. The oscillator runs at twice the LO frequency. The inductor and transistors sizes are designed using the Matlab toolbox [26].

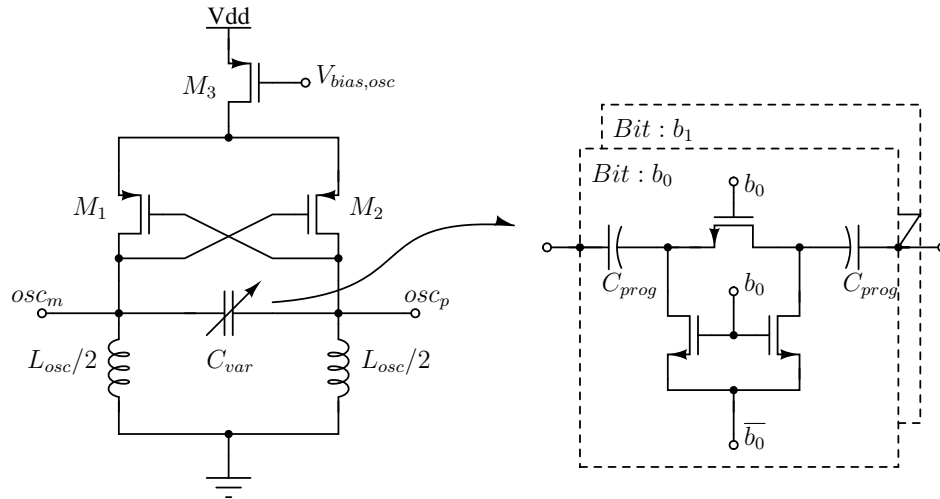


Figure 3.22: Circuit schematic of oscillator.

Two bit digital frequency programming is provided to modify the oscillation frequency by $\approx 20\%$ by using a capacitor bank as shown in Fig. 3.22.

Frequency divider The complementary sinusoidal output of the oscillator is converted to a square wave by AC coupling it to an inverter using a coupling capacitor ($C_c=1\text{pF}$) and resistor ($R_c=10\text{K}\Omega$) as shown in Fig. 3.23. The outputs of the inverters drive the clock inputs of toggle flip-flops to generate in-phase and quadrature phases. Buffers are added at the output of the flip-flops to drive the mixer and excitation coil driver switches. The digital blocks such as buffers, flip-flops, etc. are implemented using the standard cell digital library. An open drain transistor is connected to the divider outputs for off-chip frequency measurement using a bias-tee circuit and a spectrum analyser (E4408B, Agilent Technologies).

Excitation coil driver A circuit for driving the excitation coil is shown in Fig. 3.24. The centre tap of the differential excitation coil is connected to the drive voltage (V_{drive}) and the maximum current through the switches (I_0) is determined by the switch on-resistance and V_{drive} . The LO drive signals can be approximated by:

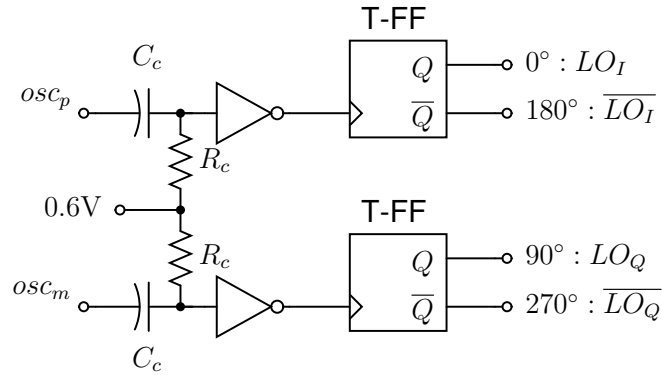


Figure 3.23: Frequency divider using toggle flip-flops (T-FF) to generate in-phase (0° and 180°) and quadrature phase (90° and 270°) LO clock signals.

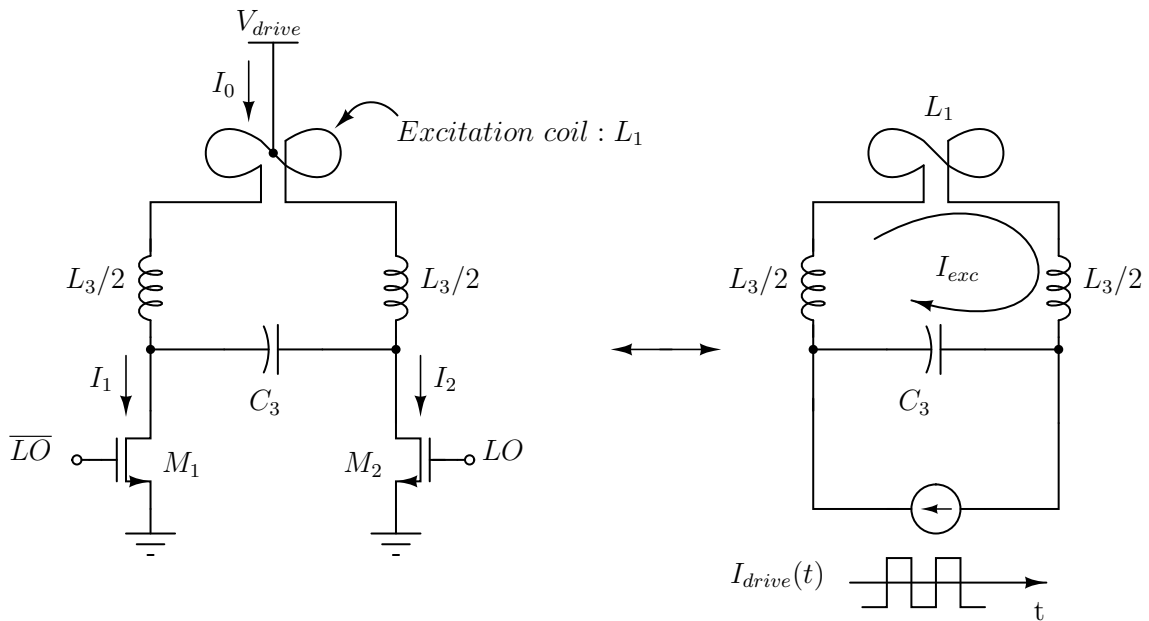


Figure 3.24: Drive circuit for excitation coil.

$$LO = \frac{1}{2} + \frac{2}{\pi} \cos \omega_{LO} t + \frac{2}{3\pi} \cos 3\omega_{LO} t + \dots \quad (3.19)$$

$$\overline{LO} = \frac{1}{2} - \frac{2}{\pi} \cos \omega_{LO} t - \frac{2}{3\pi} \cos 3\omega_{LO} t - \dots \quad (3.20)$$

The current (I_{drive}) driving the LC tank is:

$$I_{drive} = \frac{I_1 - I_2}{2} \quad (3.21)$$

$$= I_0 \frac{LO - \overline{LO}}{2} \quad (3.22)$$

$$= I_0 \left(\frac{2}{\pi} \cos \omega_{LO} t + \frac{2}{3\pi} \cos 3\omega_{LO} t + \dots \right) \quad (3.23)$$

The LC tank with a quality factor (Q) and resonance frequency (ω_{LO}), filters the higher harmonics of I_{drive} and gives a Q boost to the current in the excitation coil, thereby increasing the magnetic field intensity to magnetize the labels.

$$I_{exc} = \frac{2}{\pi} I_0 Q \cos \omega_{LO} t \quad (3.24)$$

In our design, the LC tank formed by $L_3 + L_1$ resonates at the LO frequency with an added capacitor C_3 . L_3 is implemented as a symmetric spiral inductor on M8 and M9 metal layers of the CMOS process and it is isolated from oscillator using a guard ring. Dummy metal fill ($2.1 \times 2.1 \mu\text{m}^2$) in all the metal layers is added inside the spiral to meet the fabrication constraints. The gates of the switches ($M_{1,2}$) are driven by buffered in-phase outputs of the clock divider.

Front end amplifier The front end is a trans-conductor that converts the voltage induced in the pick up coil voltage into a current using the circuit shown in Fig. 3.25. The transconductance of the input transistors ($M_{1,2}$) is set to 20mS with 2.2mA through each of them. The bias voltage (V_{bias}) to the input transistors is provided through the centre tap of the pick up coil. The gate bias of nmos current source load transistors ($M_{3,4}$) is provided by a resistive divider common mode detection circuit ($R_{CM}=3.6\text{K}\Omega$). The output current of the front end amplifier is AC coupled to the mixer using a 8pF capacitor. Here, it should be noted that the load of the front end amplifier is a low impedance node determined by the input impedance of the base-band amplifier and the on-resistance of mixer switches.

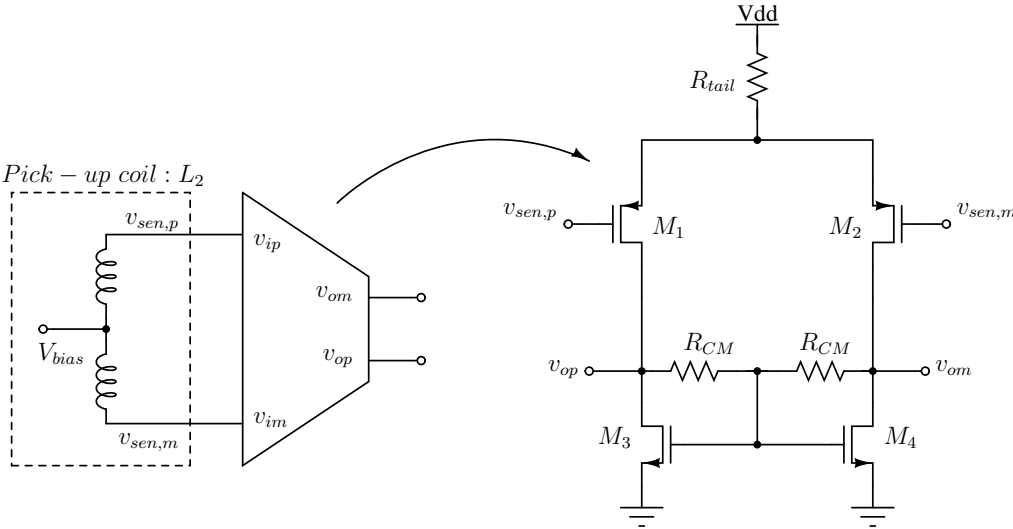


Figure 3.25: Front end amplifier circuit.

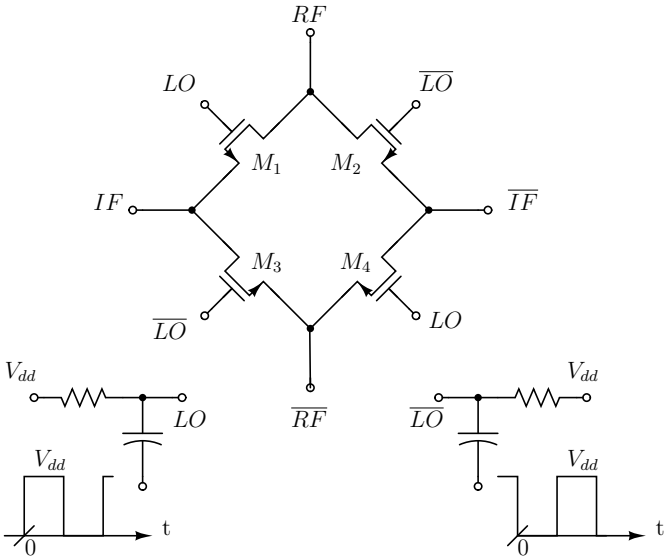


Figure 3.26: Schematic of passive mixer.

Passive mixer In a mixer, the RF signal from the front end amplifier output is multiplied by a square wave local oscillator (LO) signal to give down-converted output at IF port. For example,

$$RF = \cos(\omega_{LO} + \omega_m)t \quad (3.25)$$

$$IF = RF \cdot LO + \overline{RF} \cdot \overline{LO} \quad (3.26)$$

$$IF = \approx \frac{2}{\pi} [\cos \omega_m t + \cos(2\omega_{LO} + \omega_m)t] \quad (3.27)$$

The higher harmonic signals at mixer output can be filtered by the base-band amplifier. We have chosen a passive mixer as it is linear and has lower flicker noise compared to an active Gilbert-cell mixer. The switches of the passive mixer shown in Fig. 3.26 are implemented with nmos transistors (M_{1-4}). The square wave ($0-V_{dd}$) from the divider is AC coupled to the gates through a $8K\Omega$ resistor and $0.25pF$ capacitor. The transistors are sized to have a nominal on-resistance of 10Ω . In the layout, the mixer switches are isolated using a guard ring connected to the substrate/ground.

Base-band amplifier The base-band stage is a trans-impedance amplifier (TIA) that is realized using an operational amplifier (opamp) with a resistor ($R_F=5K\Omega$) and a capacitor ($C_F=2pF$) in feedback as shown in Fig. 3.27. The opamp is a fully differential two stage circuit with the input stage realized using nmos transistors ($M_{1,2}$). Each input transistor is biased with $0.2mA$ to give $g_m=2.2mS$. The second gain stage ($M_{6,7}$) is designed to drive a load capacitor of $10pF$ which accounts for off-chip PCB trace capacitance and off-chip gain stage input capacitance. The length of the input transistors are designed to have a flicker noise corner frequency of $8KHz$. The common mode outputs of the first stage and second stage are set using two separate common-mode feedback (CMFB) circuits. The first stage CMFB uses two differential pairs and the second stage CMFB uses a resistive divider to detect the common mode voltages respectively [27]. The stability of the opamp is ensured using miller capacitor (C_c) and series resistor (R_z) to cancel the right half plane zero. The overall TIA has input impedance of 34Ω and $3dB$ bandwidth of $660KHz$.

Feed-through cancellation As we discussed in Sec. 3.2, the pick up coil encloses the excitation coil carrying $100mA_{pp}$ current with a gap of $3\mu m$ causing an undesirable capacitive coupling between them. This steady state signal will be down-converted to a DC current by the mixer due to self mixing. The DC offset current has to be cancelled in order to prevent saturation of the base-band amplifier or subsequent amplifier stages. An external DAC is

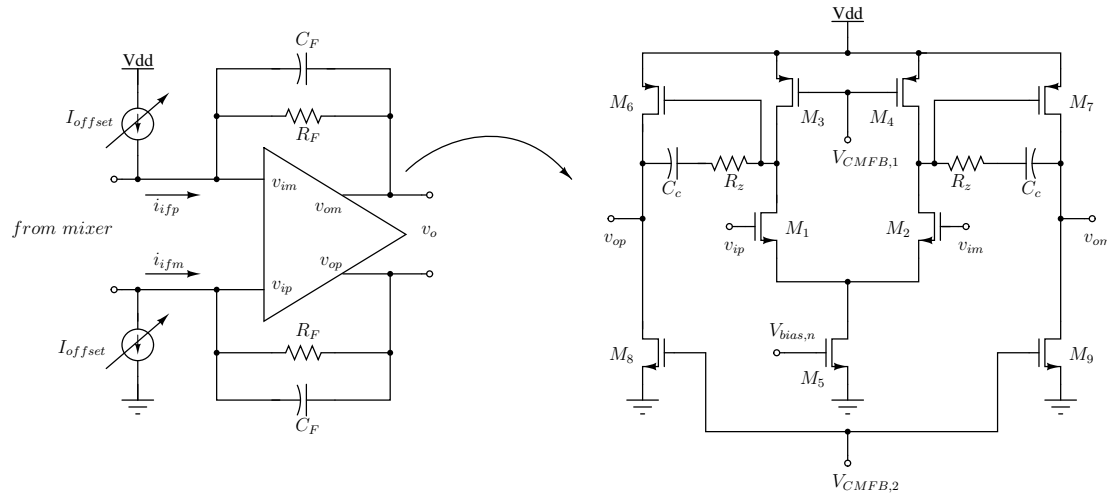


Figure 3.27: Circuit schematic of TIA and two stage differential opamp.

used to feed a programmable DC current to current mirrors connected to input of the base-band trans-impedance amplifier. Since the offset cancelling current sources are connected directly to the input of the TIA, their flicker noise directly adds to the signal current. This is avoided by choosing the channel length of $2\mu\text{m}$. A digital control bit is provided to switch the polarity of offset cancellation.

Other layout considerations The need to integrate the chip with the microfluidic channel imposes constraints on the layout design of the chip. Firstly, the pads should be only on two opposite sides of the chip so that the wire-bonds do not interfere with the microfluidic channel. Secondly, the sensor has to be placed close to the centre of the chip to avoid any leakage near the interface between the chip edge and the microfluidic channel. For multiple frequency of operation, the supply must be isolated to avoid chances of injection locking between the the receiver channels.

3.6 CMOS microfluidics integration

The chip is fabricated in TSMC65nm CMOS technology and each channel occupies $1.5 \times 0.45 \text{mm}^2$ of active chip area as shown in Fig. 3.28.

The cells are usually dispersed in a saline solution which is a conducting liquid containing ions of Na, Cl and K. However, the chip has to be connected to external biasing circuits, supply voltage and off-chip components using wire-bonds. Further the flow of cells requires

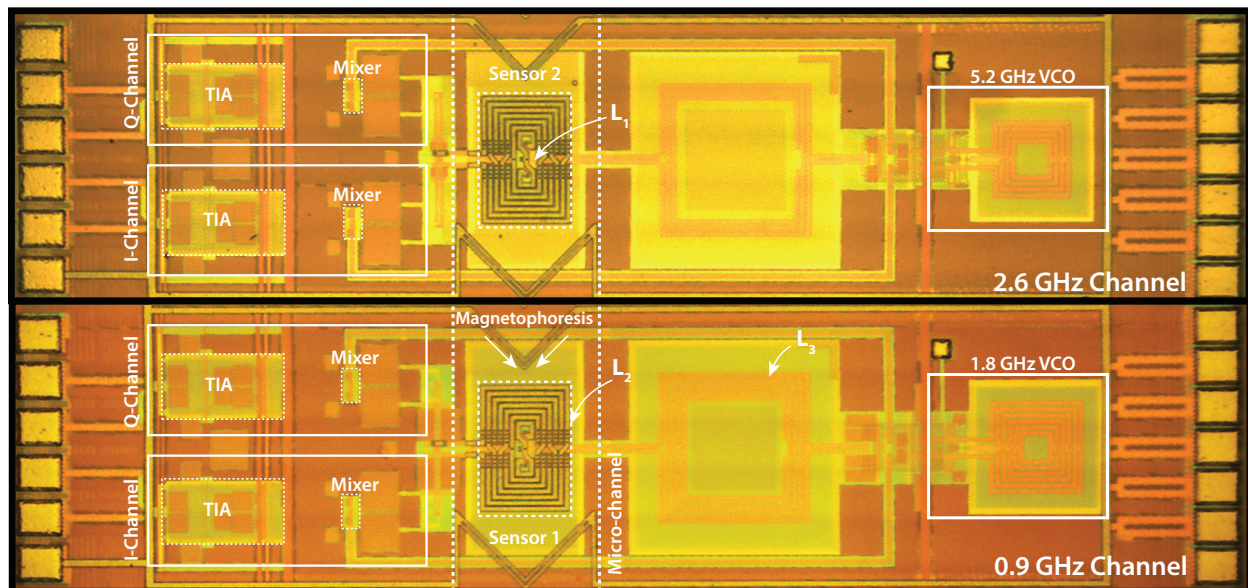


Figure 3.28: Photograph of the chip.

that the chip to be in flush with the microfluidic channel for minimum turbulence. In addition, the chip generates heat which should be dissipated out so as to limit the temperature increase to less than 37°C. The following process steps as shown in Fig. 3.29(A) are used for integrating the CMOS chip with the microfluidic channel to meet these requirements.

1. Firstly, a cavity is created in a holder ENIG-PCB. Pads are designed on either side of the cavity to provide the electrical connections through wire-bonds. The PCB is placed on a steel wafer with the pads-side facing down.
2. The CMOS chip is cleaned using iso-propyl alcohol and blow dried with nitrogen. It is then placed upside down and aligned to the centre of the cavity using laser cut polystyrene structure. After this step, conducting polymer (Coolpoly E3607) is placed in the cavity and this assembly is placed under a hot press.
3. By applying uniform pressure of 720psi from the top at a temperature of 95°C for about 5min, the conducting polymer and styrene will melt and conform with the cavity and will hold the chip in place.
4. After the setup has cooled to room temperature, the pressure is released and the CMOS+PCB is removed from the hot-embosser. The chip is wire-bonded to the PCB using aluminium bond wires. Fig. 3.29(B) shows the scanning electron microscope

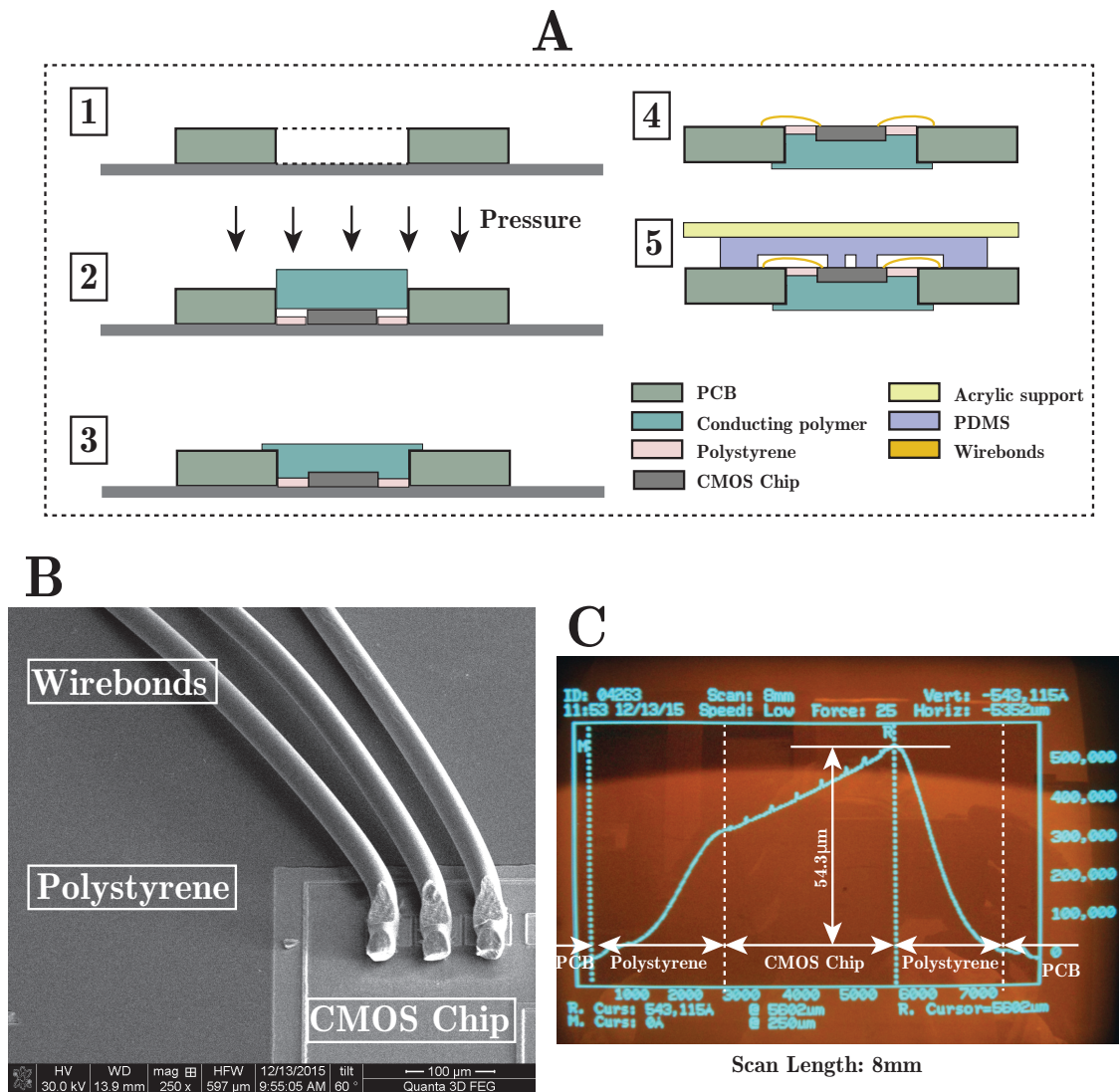


Figure 3.29: (A) Process steps for CMOS microfluidics and integration. (B) SEM image showing the interface between the CMOS chip and polystyrene. (C) Surface profile scan across the CMOS chip including the PCB and polystyrene.

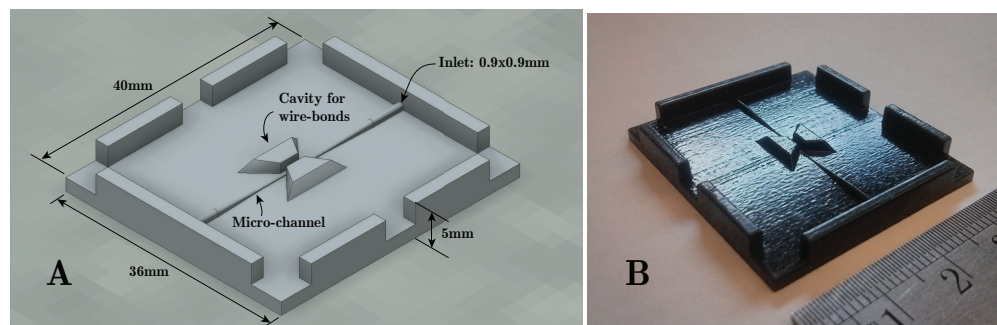


Figure 3.30: (A) CAD model of the mold showing cavities for wire-bonds. (B) 3D printed mold used for PDMS micro-channel soft-lithography.

(SEM) image of the interface between the CMOS chip and polystyrene including the wirebonds. No gaps at the interface prevents any leakage or bubble formation during flow experiments. After wire-bonding, the bond wires are covered by epoxy to isolate them from saline. Fig. 3.29(C) shows that the height variation across the PCB through polystyrene and the CMOS chip is less than $60\mu\text{m}$.

5. For fabricating the microfluidic channel, the usual approach for prototyping is to use an SU-8 molds and poly dimethyl siloxane (PDMS). In this approach, the inlet and output are punched orthogonal to the microfluidic channel. This causes the cells to settle at the inlet of the microfluidic channel interface. To avoid this problem, we have designed a 3D printed mold shown in Fig. 3.30 using rubber (Shore 60 hardness, Fathom Inc.) for the microfluidic channel. In this design, the inlet (0.9mm wide) and outlet smoothly transition to and from a $200\mu\text{m}$ wide semi-circular arch shaped microfluidic channel. The mold also has cavities for accommodating the wire-bonds. The PDMS (Sylgard 182 silicone elastomer kit) is poured into it and cured at 60°C for about five hours. The microfluidic device is removed from the mold after it has cured. Further, it is important that the microfluidic channel is hydrophilic so that the saline can fill it by wetting process. However, the PDMS is hydrophobic and requires surface treatment such as exposure to oxygen plasma that forms a thin layer of hydrophilic silanol SiOH on its surface. Therefore, we treat the PDMS with O_2 plasma for 5min with 70W power at 25°C which reduces the contact angle from 95° to 40° . The microfluidic device retains the hydrophilicity for upto 4 days when it is stored in DI-water. For flow experiments, the micro-channel is aligned over the sensors on the chip and a laser cut acrylic piece is used to press-fit the PDMS microfluidic channel against the chip to avoid any leakage as shown in Fig. 3.31(A).

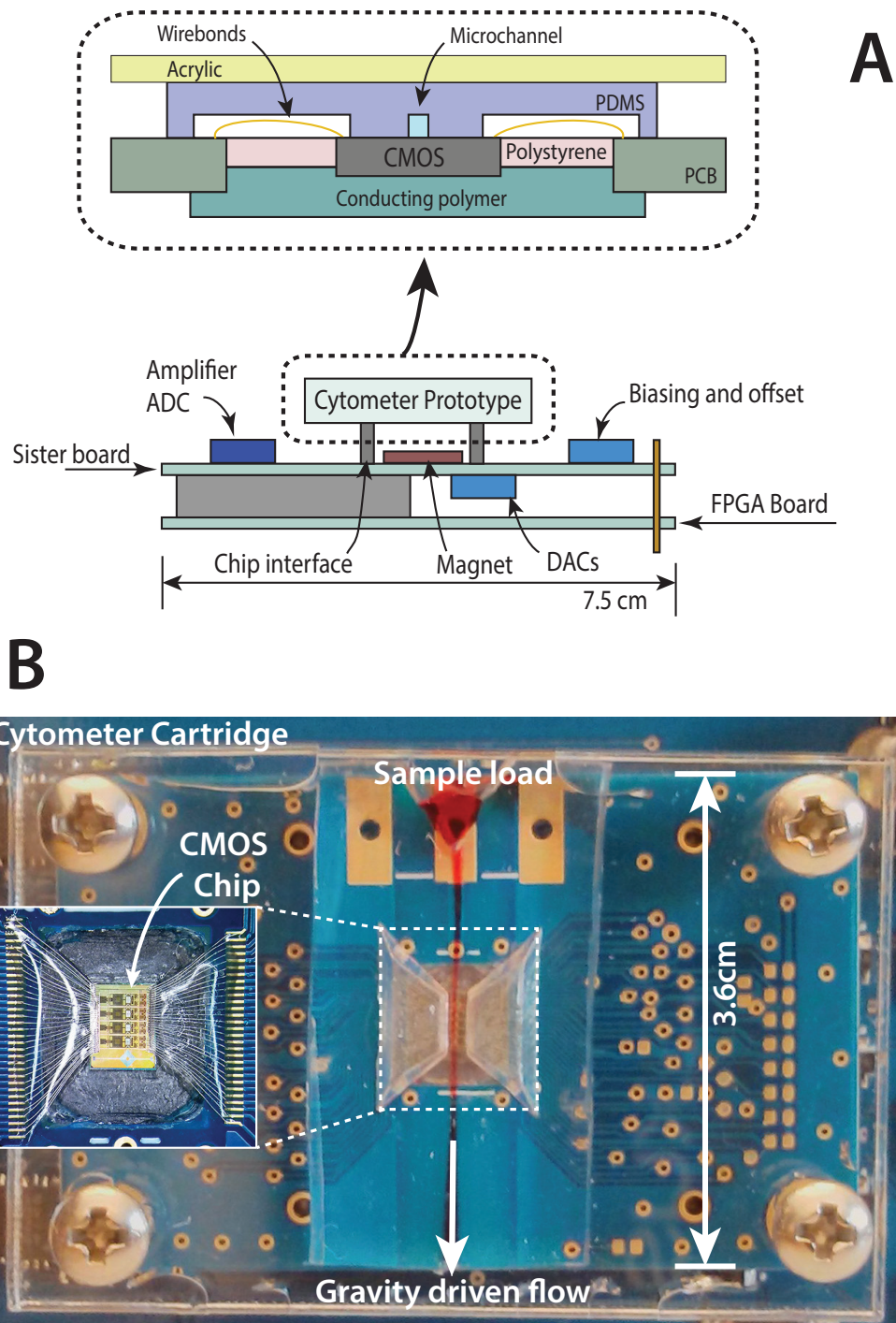


Figure 3.31: (A) Schematic of CMOS integrated with microfluidics. (B) Fabricated flow cytometer.

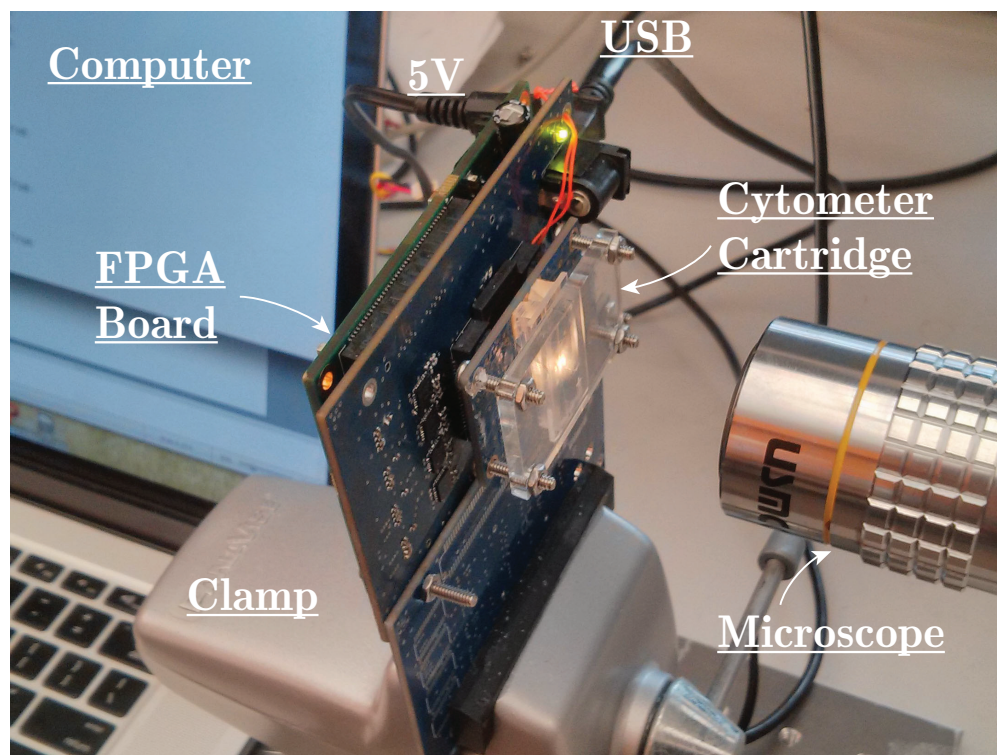


Figure 3.32: Experimental setup used for measurements.

The complete cytometer prototype is connected to a sister PCB to provide DC bias, off-chip gain, anti-alias filtering and digitization by differential ADC and data acquisition through a FPGA (OpalKelly XEM6010-LX45). A simple digital controller is implemented on the FPGA to handle DAC programming used for offset cancellation, ADC initialization. The FPGA is programmed to transfer the data to a computer through an USB port. Voltage regulators mounted on the sister PCB generate 3.3V for power the off-chip gain stages and ADCs, 1.5V for powering the CMOS chip and 1.2V for the excitation coil. A python script running on the computer acquires and saves the data from the FPGA board which is subsequently processed in Matlab. The complete experimental setup is shown in Fig. 3.32. The cytometer cartridge is firmly mounted on a clamp and powered with a 5V DC supply. The supply is shared between the OpalKelly FPGA board and the sister PCB. A USB microscope is used to visualize the flow through the micro-channel. Flow cytometry experiments are carried out by placing a drop of sample at inlet of the cytometer and it is vertically driven through the microfluidic channel by gravity. The fabricated flow cytometer is shown in Fig. 3.31(B).

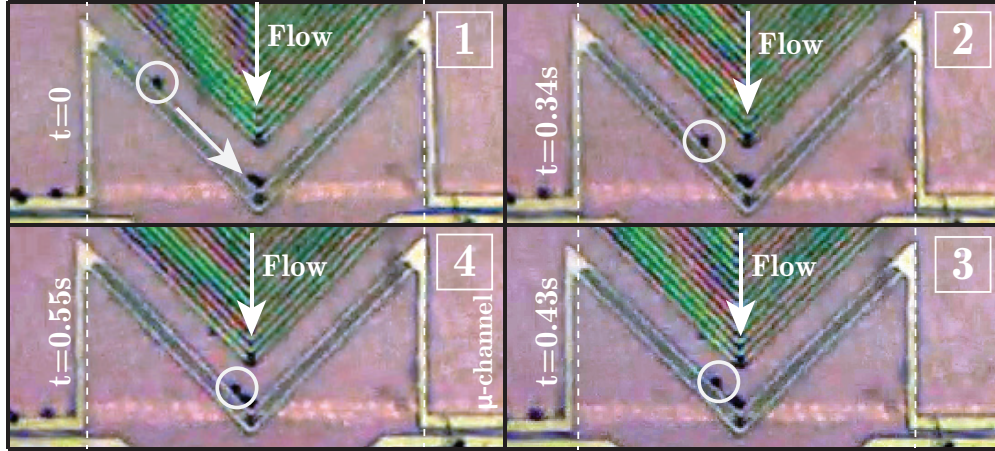


Figure 3.33: Focusing of Dynabead by magnetophoresis.

Magnetophoresis

Although a wide microfluidic channel ($200 \times 100 \mu\text{m}^2$) avoids clogging, the signal strength drops as $1/r^3$ with the particle vertically separated from the sensor by r . Additional sheath flow, a commonly used technique for focusing [28], requires well-controlled flow rates by use of external syringe pumps. The availability of magnetic labels in this application enables 3D focusing using magnetic field gradients generated from current carrying wires [29]. The force on a magnetically labeled cell with magnetic moment \vec{m} by a wire carrying a is given by:

$$\vec{F}_{mag} = (\vec{m} \cdot \nabla) \vec{B} \quad (3.28)$$

The direction of the force always points towards the wire ie. in the direction of increasing magnetic field gradient. We have used 3μ wide wires (shown in Fig. 3.33) each carrying 3.5mA, implemented on top metal layer with 45° angles. An external DC magnetic field of 5mT is used to magnetize the labels. A detailed analysis of the effect of microfluidic channel dimensions, cell diameter, liquid viscosity on the focusing efficiency of these structures will be presented in [30].

3.7 Measurement results

The receiver is powered at 1.5V supply, higher than 1.2V, which is necessary to overcome de-Qing of the oscillator LC tank due to undesired layout parasitics that were inadvertently not accounted for during simulations. The front end and opamp consumes 18mA. The excitation coil is powered at $V_{drive}=1.2V$ supply and consumes 38mA.

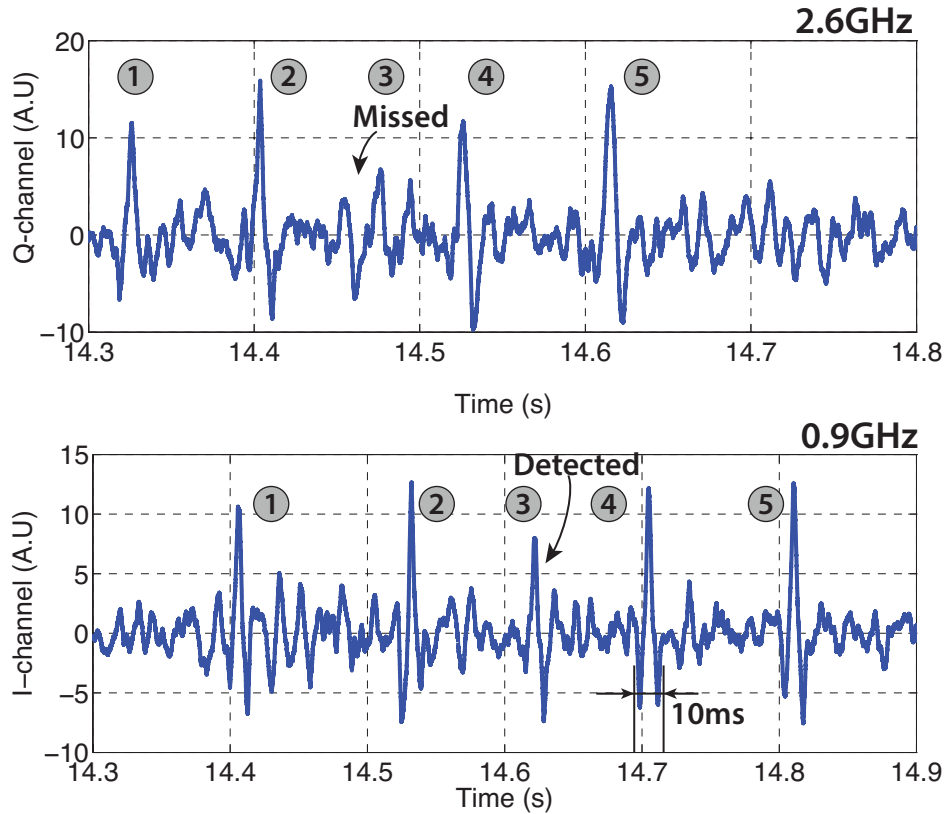


Figure 3.34: Detection of Dynabeads by two frequency channels.

Dynabead detection

Dynabeads are used for benchmarking the cytometer. Dynabeads have an average diameter of $4.5\mu\text{m}$ with well characterized magnetic properties [31]. For this experiment, these beads are dispersed in de-ionized (DI) water with a concentration of $8 \times 10^6/\text{mL}$. $50\mu\text{L}$ of DI water is loaded at the inlet of the vertically held microfluidic channel of the cytometer and the offset cancellation is performed using the external DAC as the DI water flows through the cytometer. Next, about $50\mu\text{L}$ of the Dynabead sample is loaded at the inlet and data is acquired as the particles flow over the sensor. Fig. 3.34 shows the detection of $4.5\mu\text{m}$ Dynabeads with an average SNR of 21.3dB for 0.9GHz channel and 19.9dB for 2.6GHz channel ($n=100$ particles) after matched filtering. Further, it can be seen that a particle missed on the 2.6GHz channel was picked up on the 0.9GHz channel.

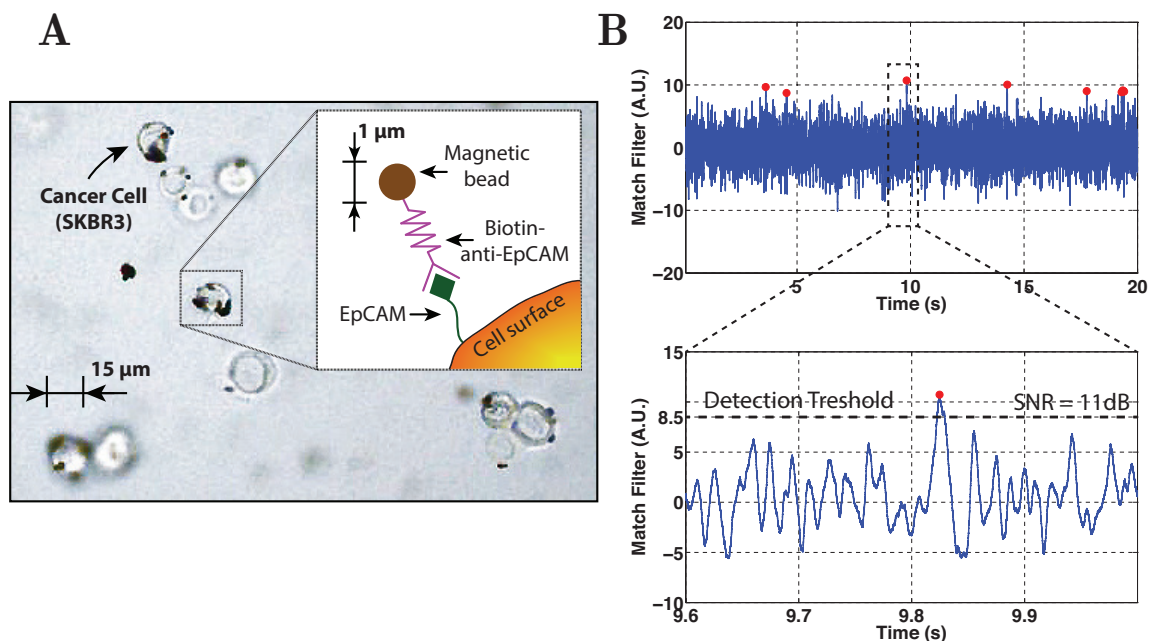


Figure 3.35: (A) Magnetic labeling of SKBR3 cells. (B) Detection of magnetically labeled cells by the cytometer.

Magnetic labelling of cells and detection

Although the design of flow cytometer is presented for neutrophil counting, the cytometer is demonstrated for detection of breast cancer cells (see Fig. 3.35(A)) as they pose minimal bio-safety hazard for handling them. Moreover, the detection of cells by the cytometer is independent of choice of cells or antibodies used for magnetic labeling as long as the SNR requirements are met. We have chosen SKBR3 breast cancer cells which over-express EpCAM antigen and have a typical diameter of 15 μm.

Biotin-streptavidin interaction is the strongest non-covalent interaction found in nature and this labeling method is routinely used in cell experiments. The labeling of cells is carried out in a two step process. Firstly, the EpCAM antigen on the cell surface is conjugated with biotinylated anti-EpCAM (CD326) antibody. The biotin is subsequently conjugated with magnetic labels coated with streptavidin.

We start with a petri dish containing about 5×10^6 SKBR3 cells. A solution buffer is prepared by mixing 2mL of 7.5% bovin serum albumin with 28mL PBS. About 2mL of 0.25% trypsin is mixed with 8mL of PBS of which 3mL is used to wash the cells and rest of it is added to the cell plate. After incubation at 37°C for 5min until most cells have detached

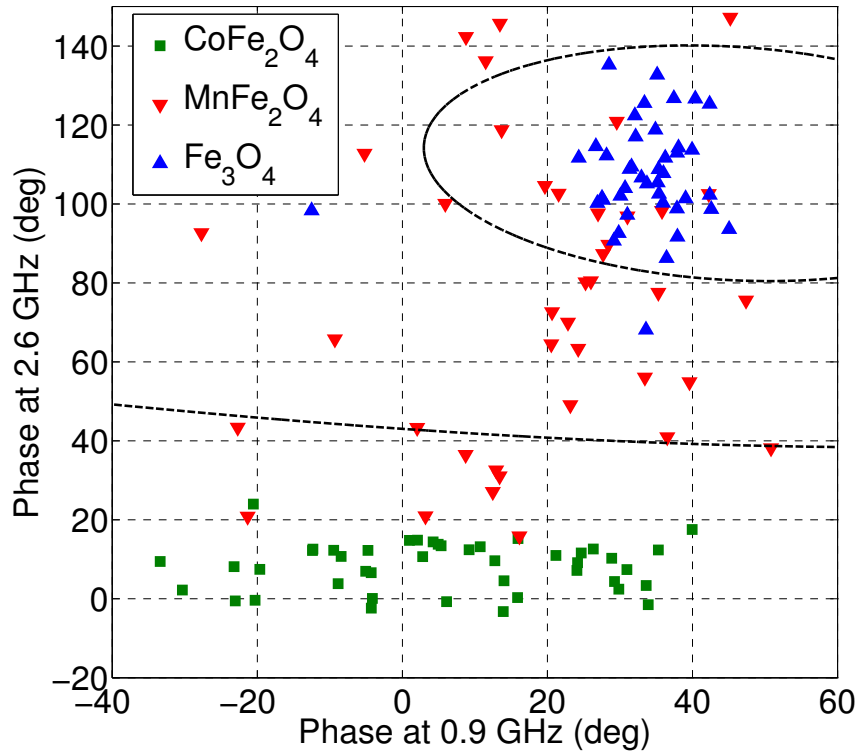


Figure 3.36: Classification of three label classes by the flow cytometer.

from the plate and the cells are transferred to a tube for centrifugation. Subsequently, the cell palette is re-suspended in a mix of $1.5\mu\text{L}$ of stock biotinylated anti-EpCAM antibody and 0.6mL of buffer solution and incubated for 20min at 37°C with gentle mixing. Now, most of the EpCAM antigens on the cell have been conjugated with biotinylated antibody. The final step of magnetic labeling is carried out by adding $15\mu\text{L}$ of 10mg/mL streptavidin coated MnFe_2O_4 magnetic labels of size $800\text{nm}-1\mu\text{m}$ (from OceanNanotech Inc.) and incubated for another 20min with gentle mixing. The cells are then used for flow cytometry experiments within 2hours. The cells are carried over the sensor in $1\times$ phosphate buffered saline solution driven by gravity. The digital data provided by the cytometer is match filtered with a pulse of 10ms duration (T_p) in Matlab. Fig. 3.35(B) shows the match filtered output. The detection threshold is set to 11dB to achieve a $\text{CV}=3.2\%$.

	2012 [32]	2012 [14]	2013 [13]	2013 [16]	This Work
Sensor	Electrode pair	μ Hall Detector	GMR	LC Tank	Spiral Transformer
Sensor integration	Off-chip	N/A	N/A	On-Chip	On-chip
External magnet	None	0.5T	0.2T	None	5mT (for focusing)
Application	Cell-counter	Flow-cytometry	Flow-cytometry	Immuno-Assay	Flow-cytometry
Label/s	None	Mn-Fe oxide	Fe oxide	Fe oxide	MnFe ₂ O ₄ , CoFe ₂ O ₄ and Fe ₂ O ₃
Separate label classes	0	3	1	2	3
Detection time	50ms	0.02ms	40ms	120s	10ms

Table 3.3: Comparison with other chip-scale immuno-sensors and flow cytometers.

Label classification

For label classification experiments, Biotin coated $8\mu\text{m}$ polymer particles, acting as cell proxies, are labeled with $1\mu\text{m}$ MnFe₂O₄ and CoFe₂O₄ magnetic labels using streptavidin-biotin chemistry and the following procedure.

Biotin-coated polymer beads with average diameter of $10\mu\text{m}$ are obtained from Bangs Laboratories Inc. The magnetic labels are functionalized with streptavidin. These labels and the beads are separately washed (vortex followed by centrifuge) with 1x phosphate buffered saline (PBS, pH 7.4). The magnetic labels are mixed with the polymer beads and incubated at 4°C for 15min. The relative concentrations of magnetic labels and polymer beads is optimized to maximize labeling efficiency (number of magnetic labels for every polymer bead). For the measurements, about $20\mu\text{L}$ of PBS is loaded at the inlet of the micro-channel. The offset current DAC is calibrated during this phase which takes about 1min. After calibration, the sample containing the magnetically labeled polymer beads is loaded at the inlet of the micro-channel. The labeled beads are carried over the sensor, driven by gravity. Unbound $1\mu\text{m}$ labels present in the sample are not detected by the detector. The data from the chip is transferred real-time to a compute and it is processed offline.

The detection threshold is set to SNR of 11dB after matched filtering. The peak amplitude of the pulse of in-phase channel (or quadrature-phase channel) that exceeds the

detection threshold is used along with the corresponding amplitude of quadrature-phase channel (or in-phase channel) to determine the phase of the signal at a particular frequency (either 0.9GHz or 2.6GHz). Fig. 3.36 shows the phase response obtained for the magnetic labels at both the frequencies. Also shown is the phase of Dynabeads beads (Fe_2O_3). Using equal prior probabilities of magnetic labels, we get classification accuracy of 74% using phase data at 2.6GHz (with linear discriminator). However, the accuracy improves to 87% by using phase data at both 0.9GHz and 2.6GHz (with a quadratic discriminator). Finally, Tab. 3.3 compares the presented flow cytometer with other chip-scale immuno-sensors and flow cytometers.

Chapter 4

Conclusion

In conclusion, we have described the need for point-of-care counting of neutrophils and the design of a CMOS sensor chip for detection of magnetically labeled cells that meets the specifications. The chip uses a spiral transformer sensor that is optimized for maximizing the SNR and the signal from it is processed using direct down-conversion receiver circuits. Two channels, operating at 0.9GHz and 2.6GHz are used to improve the SNR and classification accuracy. The CMOS chip has been successfully integrated into microfluidics using hot-embossing technique. Magneto-phoresis is used for focusing the cells onto the sensor. Dynabeads are used for benchmarking the cytometer since these magnetic particles have uniform size and magnetic properties. Cell detection is demonstrated with SKBR3 cells labeled with MnFe_2O_4 magnetic labels and EpCAM cell surface bio-markers. The cells are detected using the cytometer with SNR of 11dB to give 3.2% CV. Further, 87% classification accuracy is achieved for three magnetic label classes.

Appendix A

Gravity Driven Flow

A simplified model of the micro-channel connected to a sample reservoir is shown in Fig. A.1. The goal is to determine the time taken for the complete sample to empty through the micro-channel as a function of microchannel dimensions and surface properties.

The time of flow through the microchannel can be split into the time taken to fill (T_{fill}) the channel and the time taken for the liquid to flow through (T_{flow}). T_{fill} depends on micro-channel dimensions, the contact angle between the saline and the micro-channel, viscosity etc. and it is given by [33]:

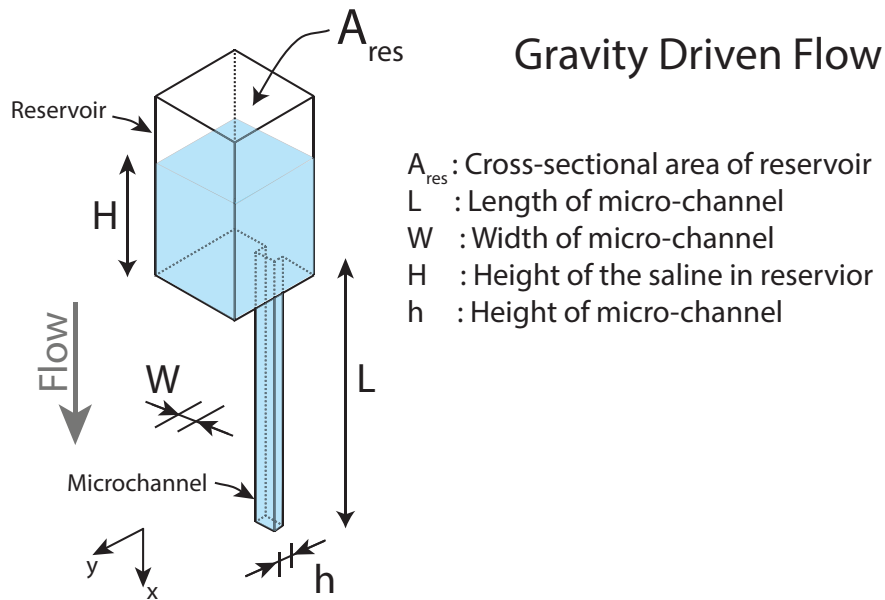


Figure A.1: Simplified schematic of a microchannel driven by gravity.

$$T_{fill} = \frac{6\eta L^2}{h^2 \rho g H + 2\sigma h \cos \theta} \quad (\text{A.1})$$

where, η is viscosity, σ is surface tension and θ is the contact angle of saline with the microfluidic channel, g is acceleration due to gravity and the remaining dimensions are shown in Fig. A.1.

Once the channel is filled, the flow is governed only by the hydrostatic pressure of the sample in the reservoir. Using the Navier-Stokes equation for the micro-channel,

$$\frac{\partial^2 u}{\partial y^2} = \frac{1}{\eta} \frac{\partial P}{\partial x} \quad (\text{A.2})$$

where $\partial P/\partial x$ is the pressure gradient, $u(y)$ is the velocity profile given by:

$$\begin{aligned} u(y) &= \frac{1}{2\eta} \left(-\frac{\partial P}{\partial x} \right) \left(\frac{h^2}{4} - y^2 \right) \\ \bar{u} &= \frac{1}{h} \int_{-h/2}^{h/2} u(y) dy = \frac{h^2}{12\eta} \left(-\frac{\partial P}{\partial x} \right) \end{aligned} \quad (\text{A.3})$$

Considering only the pressure gradient generated by the reservoir to drive the flow, we get

$$\bar{u} = \frac{h^2}{12\eta} \left(\frac{-\rho g H(t)}{L} \right) \quad (\text{A.4})$$

Using conservation of mass and the area of channel $A_{ch} = W \times h$ we have,

$$\begin{aligned} \frac{dV_{res}}{dt} &= -A_{ch} \bar{u} \\ A_{res} \frac{dH(t)}{dt} &= -A_{ch} \bar{u} \end{aligned} \quad (\text{A.5})$$

Using Eqn. A.4 and Eqn. A.5 we get,

$$H(t) = H_0 e^{-t/\beta} \quad \beta = \frac{12\eta L A_{res}}{A_{ch} \rho g h^2} \quad (\text{A.6})$$

Where H_0 is the initial height of the reservoir when sample is loaded. We need $T_{flow} = 4.5\beta$ for 99% of the sample to flow through the micro-channel.

Appendix B

Noise Analysis of Direct Down Conversion Receiver

B.1 SNR for Receiver Chain

As shown in Fig. 3.15, consider that the sensor produces bipolar signal of amplitude a_{sig} (V). Here we assume that the bandwidth of the receiver is significantly larger than the effective signal bandwidth ($\approx 5/T_p$). Let the total gain of the down-conversion receiver, off-chip amplification and digitizer be A_{tot} . The amplitude of the signal at the input of the matched filter will be $A_{tot}a_{sig}$ (V). If the input referred single sided thermal noise floor of the receiver is $N_{0,in}(V^2/Hz)$, then the thermal noise floor at the input of the matched filter is $A_{tot}^2N_{0,in}(V^2/Hz)$. If the receiver has flicker noise with a corner frequency f_c (≈ 100 KHz) the *single sided* input referred noise power spectral density of the receiver will be

$$S_{in,n}(f) = N_{0,in} \left(\frac{f_c}{f} + 1 \right) V^2/Hz \quad (\text{B.1})$$

A filter matched to the signal with a bipolar response $h(t)$ of duration T_p (≈ 10 ms) is also shown in Fig. 3.15. The signal can be represented as a scaled version of $h(t)$ where $s(t) = a_{sig}A_{tot}h(t)$. The output of the matched filter will be:

$$\begin{aligned}
 y(t) &= s(t) * h(t) \\
 &= \int_{-\infty}^{\infty} s(\tau)h(t - \tau)d\tau \\
 &= a_{sig} \int_{-\infty}^{\infty} h(\tau)h(t - \tau)d\tau \\
 \max\{y(t)\} &= \int_{-T_p/2}^{T_p/2} h^2(\tau)d\tau \\
 \max\{y(t)\} &= a_{sig}A_{tot}T_p
 \end{aligned} \tag{B.2}$$

Let $H(f)$ be the fourier transform for $h(t)$ define as follows:

$$H(f) = \int_{-\infty}^{\infty} h(t)e^{-2\pi ft} dt \tag{B.3}$$

For the given $h(t)$, it can be shown that:

$$H(f) = \frac{2}{j\pi f} \sin^2\left(\frac{\pi f T_p}{2}\right) \tag{B.4}$$

Using Eqn. B.4 and Eqn. B.1, the variance of noise at the match filter output can be calculated as follows:

$$\begin{aligned}
 \sigma_n^2 &= \int_{-\infty}^{\infty} \frac{A_{tot}^2 S_{in,n}(f)}{2} |H(f)|^2 df \\
 &= A_{tot}^2 N_{0,in} \int_0^{\infty} \left| \frac{2}{j\pi f} \sin^2\left(\frac{\pi f T_p}{2}\right) \right|^2 \cdot \left(\frac{f_c}{f} + 1\right) df \\
 &= A_{tot}^2 N_{0,in} T_p (0.693 f_c T_p + 0.5)
 \end{aligned} \tag{B.5}$$

Using Eqn. B.2 and Eqn. B.5 and noting that $f_c T_p \gg 1$ the SNR can be approximated as:

$$SNR = \frac{\max\{y(t)\}}{\sigma_n} = \frac{A_{tot} T_p a_{sig}}{\sqrt{(0.693) A_{tot}^2 N_{0,in} f_c T_p^2}} = \frac{a_{sig}}{\sqrt{(0.693) N_{0,in} f_c}} \tag{B.6}$$

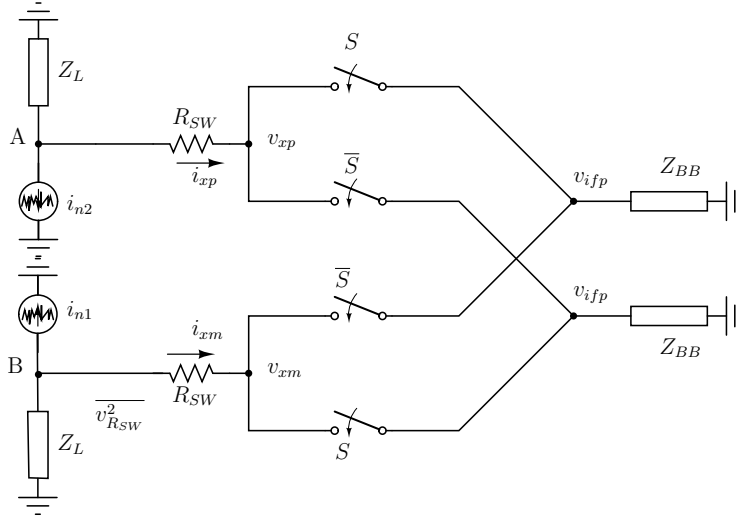


Figure B.1: Modeling of source noise of the receiver.

Receiver Noise Analysis

In this section, our goal is to evaluate the effect of different noise sources shown in Fig. 3.15, on the receiver noise performance. The passive mixer analysis presented in [34] is simplified for our narrow band receiver. Contribution of each of these noise sources to the output noise is considered in the following sections.

Noise from Front-End

Fig. B.1 shows only the noise from front end current to voltage converter ($\overline{i_n^2}$). Z_{BB} is the input impedance of the transimpedance amplifier (TIA).

$$Z_{BB} \approx R_F/A_v$$

where, R_F is the feedback resistance of the TIA and A_v is the differential voltage gain of the operational amplifier. S, \bar{S} are ideal complementary square wave (0-1) driving the mixer switches at ω_{LO} . R_{SW} is the resistance of passive mixer switches. $Z_L = 1/Y_L$ is evaluated at the LO frequency (0.9GHz) and it is assumed to be constant across the bandwidth of the sensor signal (± 100 KHz). Writing the KCL at nodes A and B,

$$\begin{aligned} i_{n1} + Y_L(v_{xp} + i_{xp}R_{SW}) + i_{xp} &= 0 \\ i_{n2} + Y_L(v_{xm} + i_{xm}R_{SW}) + i_{xm} &= 0 \end{aligned}$$

From above equations we get,

$$(v_{xp} - v_{xm})Y_L + (i_{xp} - i_{xm})(R_{SW}Y_L + 1) + i_{n1} - i_{n2} = 0 \quad (\text{B.7})$$

Also,

$$\begin{aligned} v_{xp} &= v_{ifp}S + v_{ifm}\bar{S} \\ v_{xm} &= v_{ifp}\bar{S} + v_{ifm}S \\ v_{xp} - v_{xm} &= (v_{ifp} - v_{ifm})(S - \bar{S}) \end{aligned} \quad (\text{B.8})$$

Substituting Eqn. B.8 in Eqn. B.7 we get:

$$i_{xp} - i_{xm} = - \left[\frac{(i_{n1} - i_{n2} - (v_{ifp} - v_{ifm})(S - \bar{S})Y_L)}{(1 + R_{SW}Y_L)} \right] \quad (\text{B.9})$$

Further,

$$\begin{aligned} i_{ifp} &= i_{xp}S + i_{xm}\bar{S} \\ i_{ifm} &= i_{xp}\bar{S} + i_{xm}S \\ i_{if} &= \frac{i_{ifp} - i_{ifm}}{2} \\ i_{if}(t) &= \frac{1}{2}(i_{xp} - i_{xm})(S - \bar{S}) \end{aligned} \quad (\text{B.10})$$

From Eqn. B.9 and Eqn. B.10 and since $(S - \bar{S})^2 = 1$ we get:

$$i_{if}(t) = -\frac{1}{2} \left[\frac{(i_{n1} - i_{n2})(S - \bar{S} + Y_L(v_{ifp} - v_{ifm}))}{1 + R_{SW}Y_L} \right] \quad (\text{B.11})$$

In the frequency domain $(S - \bar{S} \leftrightarrow S(\omega))$,

$$\begin{aligned} V_{ifp}(\omega) - V_{ifm}(\omega) &= 2Z_{BB}I_{if}(\omega) \\ V_{ifp}(\omega) - V_{ifm}(\omega) &= -\frac{Z_{BB}}{1 + R_{SW}Y_L} [(I_{n1}(\omega) - I_{n2}(\omega)) * S(\omega) + Y_L(V_{ifp}(\omega) - V_{ifm}(\omega))] \\ V_{ifp}(\omega) - V_{ifm}(\omega) &= -\frac{Z_{BB}}{1 + Z_{BB}Y_L + R_{SW}Y_L} (I_{n1}(\omega) - I_{n2}(\omega)) * S(\omega) \end{aligned} \quad (\text{B.12})$$

Substituting Eqn. B.12 in Eqn. B.11 and after further simplification we get,

$$I_{IF}(\omega) = -\frac{1}{2} \left[\frac{Z_L}{Z_L + R_{SW} + Z_{BB}} \right] I_{nt}(\omega) \quad (\text{B.13})$$

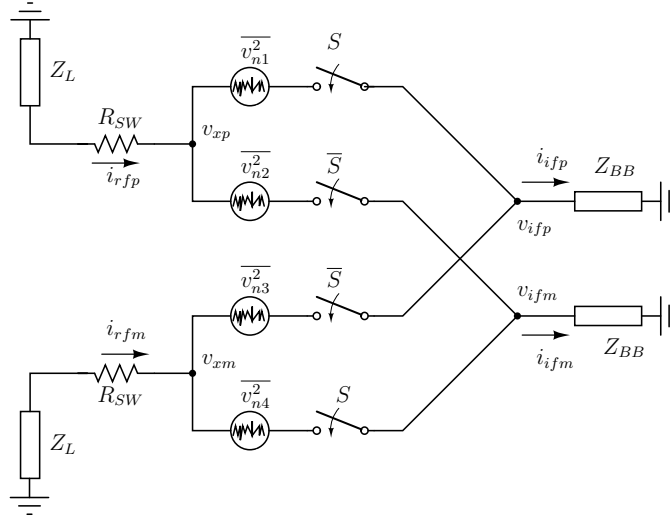


Figure B.2: Modeling of noise from the switches.

where $I_{nt}(\omega) = (I_{n1}(\omega) - I_{n2}(\omega)) * S(\omega)$, considering only the fundamental of the square wave driving the mixer,

$$S(\omega) \approx \frac{2}{\pi} (\delta(\omega - \omega_{LO}) + \delta(\omega + \omega_{LO}))$$

$$I_{nt}(\omega) * S(\omega) = \frac{2}{\pi} [I_{n1}(\omega - \omega_{LO}) + I_{n1}(\omega + \omega_{LO}) + I_{n2}(\omega - \omega_{LO}) + I_{n2}(\omega + \omega_{LO})] \quad (\text{B.14})$$

The double sided thermal noise power from the source can be represented by power spectral density $\overline{i_{n1,n2}^2}/2$:

$$S_{I_{nt}} = 4 \left(\frac{2}{\pi} \right)^2 \left(\frac{\overline{i_{ns}^2}}{2} \right) \quad (\text{B.15})$$

Substituting Eqn. B.15 in Eqn. B.13 to find the single sided noise current power spectral density at the input of the TIA is given by:

$$S_{I_{IF}}^{src}(\omega) = \left(\frac{2}{\pi} \right)^2 \left| \frac{Z_L}{Z_L + R_{SW} + Z_{BB}} \right|^2 \overline{i_{n1,n2}^2} \quad (\text{B.16})$$

Passive Mixer Noise

The switch resistance thermal noise is modeled by $\overline{v_{R_{SW}}^2} = \overline{v_{n1-n4}^2}$ as shown in Fig. B.2.

$$\begin{aligned} v_{xp} &= -i_{xp}(R_{SW} + Z_L) \\ v_{xm} &= -i_{xm}(R_{SW} + Z + L) \end{aligned} \quad (\text{B.17})$$

Also,

$$\begin{aligned}
 i_{ifp} &= i_{xp}S + i_{xm}\bar{S} \\
 i_{ifm} &= i_{xm}\bar{S} + i_{xp}S \\
 i_{if} &= \frac{i_{ifp} - i_{ifm}}{2} = \frac{i_{xp} - i_{xm}}{2}(S - \bar{S})
 \end{aligned} \tag{B.18}$$

Using Eqn. B.17 in Eqn. B.18, we get

$$i_{if}(t) = -\frac{1}{2} \frac{1}{R_{SW} + Z_L} (v_{xp} - v_{xm})(S - \bar{S}) \tag{B.19}$$

Now,

$$\begin{aligned}
 v_{xp} &= (v_{ifp} + v_{n1})S + (v_{ifm} + v_{n2})\bar{S} \\
 v_{xm} &= (v_{ifp} + v_{n3})\bar{S} + (v_{ifm} + v_{n3})S \\
 v_{xp} - v_{xm} &= (v_{ifp} - v_{ifm})(S - \bar{S}) + (v_{n1} - v_{n4})S + (v_{n2} - v_{n3})\bar{S}
 \end{aligned} \tag{B.20}$$

Substituting Eqn. B.20 in Eqn. B.19 and since $(S - \bar{S})^2 = 1$ we get,

$$i_{if}(t) = -\frac{1}{2} \frac{1}{Z_L + R_{SW}} \left[(v_{ifp} - v_{ifm}) + (v_{n1} - v_{n4})(S^2 - S\bar{S}) + (v_{n2} - v_{n3})(\bar{S}^2 - S\bar{S}) \right] \tag{B.21}$$

We know that $S\bar{S} = 0$ and $S^2 = S$ and $\bar{S}^2 = \bar{S}$, the above equation simplifies to:

$$i_{if}(t) = -\frac{1}{2} \frac{1}{Z_L + R_{SW}} \left[(v_{ifp} - v_{ifm}) + (v_{n1} - v_{n4})S + (v_{n2} - v_{n3})\bar{S} \right] \tag{B.22}$$

A square wave for S (0 to 1) can be represented as,

$$S = \frac{1}{2} + \frac{2}{\pi} \cos \omega_{LO}t + \frac{2}{3\pi} \cos 3\omega_{LO}t + \dots \tag{B.23}$$

$$\bar{S} = \frac{1}{2} - \left(\frac{2}{\pi} \cos \omega_{LO}t + \frac{2}{3\pi} \cos 3\omega_{LO}t + \dots \right) \tag{B.24}$$

Considering only the fundamental of the square wave, we can represent S, \bar{S} in frequency domain as:

$$S(\omega) = \frac{1}{2} + \frac{1}{\pi} [\delta(\omega - \omega_{LO}) + \delta(\omega + \omega_{LO})] \tag{B.25}$$

$$\bar{S}(\omega) = \frac{1}{2} - \frac{1}{\pi} [\delta(\omega - \omega_{LO}) + \delta(\omega + \omega_{LO})] \tag{B.26}$$

$$\tag{B.27}$$

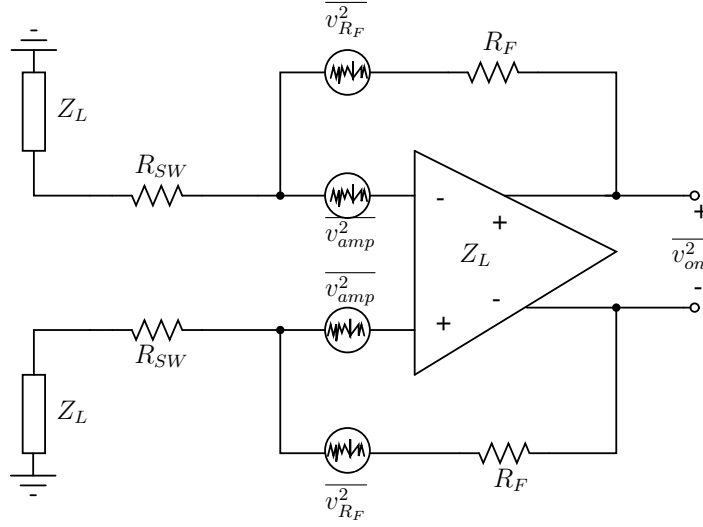


Figure B.3: Modeling of base-band noise sources of the receiver.

Further,

$$V_{ifp}(\omega) - V_{ifm}(\omega) = 2Z_{BB}I_{IF}(\omega) \quad (\text{B.28})$$

Using frequency domain form of Eqn. B.22 in Eqn. B.28 we get:

$$\begin{aligned} I_{if}(\omega) &= -\frac{1}{2} \frac{1}{Z_L + R_{SW} + Z_{BB}} \left[(V_{n1}(\omega) - V_{n4}(\omega)) * S(\omega) + ((V_{n2}(\omega) - V_{n3}(\omega)) * \overline{S(\omega)}) \right] \\ I_{if}(\omega) &= -\frac{1}{2} \frac{1}{Z_L + R_{SW} + Z_{BB}} V_n(\omega) \\ S_{IIF}^{R_{SW}}(\omega) &= \frac{1}{4} \left| \frac{1}{Z_L + R_{SW} + Z_{BB}} \right|^2 S_{V_n}(\omega) \end{aligned} \quad (\text{B.29})$$

where,

$$\begin{aligned}
 V_n(\omega) &= \left[(V_{n1}(\omega) - V_{n4}(\omega)) * S(\omega) + ((V_{n2}(\omega) - V_{n3}(\omega)) * \overline{S(\omega)}) \right] \\
 &= (V_{n1}(\omega) - V_{n4}(\omega)) * \left[\frac{1}{2} + \frac{1}{\pi}(\delta(\omega - \omega_{LO}) + \delta(\omega + \omega_{LO})) \right] \\
 &\quad + (V_{n2}(\omega) - V_{n3}(\omega)) * \left[\frac{1}{2} - \frac{1}{\pi}(\delta(\omega - \omega_{LO}) + \delta(\omega + \omega_{LO})) \right] \\
 &= \frac{1}{2}(V_{n1}(\omega) - V_{n4}(\omega) + V_{n2}(\omega) - V_{n3}(\omega)) \\
 &\quad + \frac{1}{\pi} [V_{n1}(\omega - \omega_{LO}) + V_{n1}(\omega + \omega_{LO}) - V_{n4}(\omega - \omega_{LO}) - V_{n4}(\omega + \omega_{LO})] \\
 &\quad - \frac{1}{\pi} [V_{n2}(\omega - \omega_{LO}) + V_{n2}(\omega + \omega_{LO}) - V_{n3}(\omega - \omega_{LO}) - V_{n3}(\omega + \omega_{LO})] \\
 S_{V_n}(\omega) &= 4 \left(\frac{1}{2} \right)^2 (2k_B T R_{SW}) + 8 \left(\frac{1}{\pi} \right)^2 (2k_B T R_{SW}) \tag{B.30}
 \end{aligned}$$

Using Eqn. B.30 in Eqn. B.29, the single sided noise spectral density from the switch resistance is:

$$S_{I_{IF}}^{R_{SW}}(\omega) = \left| \frac{1}{Z_L + R_{SW} + Z_{BB}} \right|^2 \left(\frac{1}{2^2} + \frac{2}{\pi^2} \right) \overline{v_{R_{SW}}^2} \tag{B.31}$$

where $\overline{v_{R_{SW}}^2} = 4k_B T R_{SW}$.

Base-band Noise

Either of the switches S or \overline{S} will be ON at any given time, therefore the receiver can be modeled as shown in Fig. B.3.

$\overline{v_{R_F}^2}$ is the noise from the feedback resistor R_F and $\overline{v_{amp}^2}$ is the input referred noise from operation amplifier. From circuit analysis, assuming A_v to be large, it can be shown that:

$$S_{v_{on}}^{BB}(\omega) = 2\overline{v_{R_F}^2} + 2 \left| 1 + \frac{R_F}{Z_L + R_{SW}} \right| \overline{v_{amp}^2} \tag{B.32}$$

Combining Eqn. B.16, Eqn. B.31 and Eqn. B.32, the total output noise spectral density of the receiver is:

$$S_{v_{on}} = S_{v_{on}}^{BB} + (2R_F)^2 [S_{I_{IF}}^{src} + S_{I_{IF}}^{R_{SW}}] \tag{B.33}$$

Bibliography

- [1] Arun Manickam et al. “A CMOS electrochemical impedance spectroscopy (EIS) biosensor array”. In: *Biomedical Circuits and Systems, IEEE Transactions on* 4.6 (2010), pp. 379–390.
- [2] Kang-Ho Lee et al. “CMOS capacitive biosensor with enhanced sensitivity for label-free DNA detection”. In: *Solid-State Circuits Conference Digest of Technical Papers (ISSCC), 2012 IEEE International*. IEEE. 2012, pp. 120–122.
- [3] Turgut Aytur et al. “A novel magnetic bead bioassay platform using a microchip-based sensor for infectious disease diagnosis”. In: *Journal of immunological methods* 314.1 (2006), pp. 21–29.
- [4] Flavio Heer et al. “CMOS electro-chemical DNA-detection array with on-chip ADC”. In: *Solid-State Circuits Conference, 2008. ISSCC 2008. Digest of Technical Papers. IEEE International*. IEEE. 2008, pp. 168–604.
- [5] David T Miyamoto, Lecia V Sequist, and Richard J Lee. “Circulating tumour cells [mdash] monitoring treatment response in prostate cancer”. In: *Nature Reviews Clinical Oncology* (2014).
- [6] *Frequencies of Cell Types in Human Peripheral Blood*. http://www.stemcell.com/~media/Files/wallchart_CellTypes_WEB.pdf. Accessed: 2015-11-15.
- [7] *Scepter 2.0 Handheld Automated Cell Counter*. https://www.emdmillipore.com/US/en/life-science-research/cell-analysis/scepter-cell-counter/w2ib.qB.Ly4AAAE_Pc1kifKu,nav. Accessed: 2015-11-15.
- [8] *When Physiology Shapes Anatomy, Lifespan of Body Parts*. <http://www.medicalsciencenavigator.com/physiology-of-self-renewal>. Accessed: 2015-11-21.
- [9] Frances Talaska Fischbach and Marshall Barnett Dunning. *A manual of laboratory and diagnostic tests*. Lippincott Williams & Wilkins, 2009.

- [10] *BC-5000 Auto Hematology Analyzer*. <http://www.mindray.com/en/products/BC-5000.html>. Accessed: 2015-12-11.
- [11] Mauro Buttarello. “Quality specification in haematology: the automated blood cell count”. In: *Clinica Chimica Acta* 346.1 (2004), pp. 45–54.
- [12] Lloyd A Currie. “Limits for qualitative detection and quantitative determination. Application to radiochemistry”. In: *Analytical chemistry* 40.3 (1968), pp. 586–593.
- [13] Michael Helou et al. “Time-of-flight magnetic flow cytometry in whole blood with integrated sample preparation”. In: *Lab on a Chip* 13.6 (2013), pp. 1035–1038.
- [14] David Issadore et al. “Ultrasensitive clinical enumeration of rare cells ex vivo using a micro-hall detector”. In: *Science translational medicine* 4.141 (2012), 141ra92–141ra92.
- [15] Simone Gambini et al. “A CMOS 10kpixel baseline-free magnetic bead detector with column-parallel readout for miniaturized immunoassays”. In: *Solid-State Circuits Conference Digest of Technical Papers (ISSCC), 2012 IEEE International*. IEEE. 2012, pp. 126–128.
- [16] Constantine Sideris and Ali Hajimiri. “An integrated magnetic spectrometer for multiplexed biosensing”. In: *Solid-State Circuits Conference Digest of Technical Papers (ISSCC), 2013 IEEE International*. IEEE. 2013, pp. 300–301.
- [17] PC Fannin. “Wideband measurement and analysis techniques for the determination of the frequency-dependent, complex susceptibility of magnetic fluids”. In: *Advances in chemical physics* 104 (1998), pp. 181–292.
- [18] Charles J O’Connor. “Magnetic-Susceptibility Measurement Techniques”. In: *ACS Symposium Series*. Vol. 644. 1996, pp. 44–66.
- [19] Sunderarajan S Mohan et al. “Simple accurate expressions for planar spiral inductances”. In: *Solid-State Circuits, IEEE Journal of* 34.10 (1999), pp. 1419–1424.
- [20] C Patrick Yue and S Simon Wong. “Physical modeling of spiral inductors on silicon”. In: *Electron Devices, IEEE Transactions on* 47.3 (2000), pp. 560–568.
- [21] A Stogryn. “Equations for calculating the dielectric constant of saline water (correspondence)”. In: *IEEE transactions on microwave theory and Techniques* (1971), pp. 733–736.
- [22] Asad Abidi et al. “Direct-conversion radio transceivers for digital communications”. In: *Solid-State Circuits, IEEE Journal of* 30.12 (1995), pp. 1399–1410.

- [23] Behzad Razavi. “Design considerations for direct-conversion receivers”. In: *Circuits and Systems II: Analog and Digital Signal Processing, IEEE Transactions on* 44.6 (1997), pp. 428–435.
- [24] Richard Przybyla. “Ultrasonic 3D Rangefinder on a Chip”. PhD thesis. EECS Department, University of California, Berkeley, May 2015. URL: <http://www.eecs.berkeley.edu/Pubs/TechRpts/2015/EECS-2015-27.html>.
- [25] *Essential Markers*. http://www.biolegend.com/essential_markers. Accessed: 2015-10-25.
- [26] Stephen Boyd, Seung Jean Kim, and S Mohan. “Geometric programming and its applications to EDA problems”. In: *date tutorial* (2005).
- [27] Paul R Gray et al. *Analysis and design of analog integrated circuits*. Wiley, 2001.
- [28] Chien Jun-Chau et al. “A 6.5/11/17.5/30-GHz high throughput interferometer-based reactance sensors using injection-locked oscillators and ping-pong nested chopping”. In: *VLSI Circuits Digest of Technical Papers, 2014 Symposium on*. IEEE. 2014, pp. 1–2.
- [29] V Iyer et al. “Encapsulation of integrated circuits in plastic microfluidic systems using hot embossing”. In: *Solid-State Sensors, Actuators and Microsystems (TRANSDUCERS), 2015 Transducers-2015 18th International Conference on*. IEEE. 2015, pp. 1822–1825.
- [30] Matthias Auf der Mauer. “Magento-phoresis in Microfluidic Devices”. MA thesis. Switzerland: Eidgenoessische Technische Hochschule Zurich, 2016.
- [31] Geir Fønnum et al. “Characterisation of Dynabeads by magnetization measurements and Mössbauer spectroscopy”. In: *Journal of Magnetism and Magnetic Materials* 293.1 (2005), pp. 41–47.
- [32] Kang-Ho Lee et al. “A CMOS impedance cytometer for 3D flowing single-cell real-time analysis with Δ - Σ error correction”. In: *Solid-State Circuits Conference Digest of Technical Papers (ISSCC), 2012 IEEE International*. IEEE. 2012, pp. 304–306.
- [33] WR Jong et al. “Flows in rectangular microchannels driven by capillary force and gravity”. In: *International Communications in heat and Mass transfer* 34.2 (2007), pp. 186–196.

- [34] Siva Thyagarajan. “Millimeter-wave/terahertz circuits and systems for wireless communication”. PhD thesis. EECS Department, University of California, Berkeley, May 2014. URL: <http://www.eecs.berkeley.edu/Pubs/Dissertations/Faculty/niknejad.html>.